Rotating nuclei: from ground state to the extremes of spin and deformation

A. V. Afanasjev[1]

[1] *Department of Physics and Astronomy, Mississippi State University, MS 39762*

(Dated: October 29, 2015)

The rotating nuclei represent one of most interesting subjects for theoretical and experimental studies. They open a new dimension of nuclear landscape, namely, spin direction. Contrary to the majority of nuclear systems, their properties sensitively depend on time-odd mean fields and currents in density functional theories. Moreover, they show a considerable interplay of collective and single-particle degrees of freedom. In this chapter, I discuss the basic features of the description of rotating nuclei in one-dimensional cranking approximation of covariant density functional theory. The successes of this approach to the description of rotating nuclei at low spin in pairing regime and at high spin in unpaired regime in wide range of deformations (from normal to hyperdeformation) are illustrated. I also discuss the recent progress and open questions in our understanding of the role of proton-neutron pairing in rotating nuclei at $N \approx Z$, the physics of band termination and other phenomena in rotating nuclei.

PACS numbers: 21.10.Jx, 21.10.Pc, 21.60.Jz, 27.70.+j, 27.70.+q

arXiv:1510.08400v1 [nucl-th] 28 Oct 2015

CONTENTS

I. Introduction 2

II. One-dimensional cranking approximation 2

III. Time-odd mean fields in rotating nuclei 6

IV. Currents in the intrinsic (rotating) frame 11

V. Ground state rotational bands in normal-deformed even-even nuclei 13

VI. Rotational bands of odd-mass nuclei in paired regime 17

VII. Hyperdeformation at high spin 19

VIII. Other phenomena 24
A. Superdeformation in paired and unpaired regimes 25
B. Neutron-proton pairing 27
C. Band termination 27
D. Other results 28

IX. Conclusions 28

References 29

I. INTRODUCTION

The development of self-consistent many-body theories aiming at the description of low-energy nuclear phenomena provides the necessary theoretical tools for an exploration of the nuclear chart into known and unknown regions. Theoretical methods (both relativistic [1] and non-relativistic [2]) formulated within the framework of density functional theory (DFT) are the most promising tools for the global investigation of the properties of atomic nuclei. The power of the DFT models is essentially unchallenged in medium and heavy mass nuclei where 'ab-initio' type few-body calculations are computationally impossible and the applicability of spherical shell model is restricted to a few regions in the vicinity of doubly shell closures.

One can consider a nuclear chart as three-dimensional object in which the charge, isospin and spin play a role of the coordinates. The studies of superheavy and neutron-rich nuclei allow to extend this chart in the directions of the charge and isospin, respectively. On the other hand, the investigations of rotating nuclei explore nuclear chart in the spin direction. Over the decades, the studies of rotating nuclei have revealed a lot of new interesting nuclear phenomena such as superdeformation [3], smooth band termination [4], magnetic rotation [5] etc. Many of them can be succesfully studied in the framework of one-dimensional cranking approximation [1]. The realization of this approximation in the framework of covariant density functional theory (CDFT) and its application to rotating nuclei in different regimes of spin, deformation and pairing and in different regions of nuclear chart are reviewed in the present paper. This review mostly focuses on the physical phenomena which were studied from 2005 since pre-2005 studies of rotating nuclei in the CDFT have been overviewed in Ref. [1]. However, few examples of the studies of rotating nuclei from this time period are given in Sect. VIII for a completeness of the picture.

II. ONE-DIMENSIONAL CRANKING APPROXIMATION

The description of rotating nuclei requires a transformation of the relativistic Hartree-Bogoliubov (RHB) equations to the rotating frame. The concept of a frame, which rotates around a fixed axis with constant rotational frequency Ω, is not strictly compatible with Lorentz invariance because a rotating frame is an accelerated rather than an inertial one. Strictly speaking such a problem should be treated in the framework of general relativity. However, one can also

[1] The review of two- and three-dimensional cranking approximations in the CDFT is presented in Ref. [6] and in Chapter 9 of this book.

look on this problem differently. Points connected with such a frame move with the velocity $r\Omega$, where r is the distance of such a point from the axis of rotation. In nuclei the relevant distances r are not much larger than the nuclear radius R. Since rotational frequencies in nuclei usually do not exceed $\Omega \sim 1-2$ MeV, the linear velocities at the surface of rotating nuclei are of the order of only a few percents of the velocity of light. Therefore, the effects of general relativity can be neglected and we just have to transform the system to a coordinate frame rotating with constant rotational frequency Ω. Such transformations have been studied in detail within the semi-classical approximation [7], within the formalism of special relativity [8] and with techniques of general relativity [9]. All these investigations lead to identical results.

The transformation of the RHB equations to the rotating frame leads to the cranked RHB (CRHB) equations [10, 11]. Note that in the present manuscript only one-dimensional rotation with rotational frequency Ω_x around x-axis (*one-dimensional cranking approximation*) is considered. Their nucleonic part has the form

$$\begin{pmatrix} \hat{h}_D - \lambda_\tau - \Omega_x \hat{j_x} & \hat{\Delta} \\ -\hat{\Delta}^* & -\hat{h}_D^* + \lambda_\tau + \Omega_x \hat{j_x}^* \end{pmatrix} \begin{pmatrix} U(\mathbf{r}) \\ V(\mathbf{r}) \end{pmatrix}_k = E_k \begin{pmatrix} U(\mathbf{r}) \\ V(\mathbf{r}) \end{pmatrix}_k \tag{1}$$

with the chemical potentials λ_τ ($\tau = n, p$) for neutrons and protons and the single-particle angular momentum operators $\hat{j_x}$ for fermions with spin $\frac{1}{2}$. The Dirac Hamiltonian $\hat{h}_D$

$$\hat{h}_D = \boldsymbol{\alpha}(-i\boldsymbol{\nabla} - \boldsymbol{V}(\mathbf{r})) \; + \; V_0(\mathbf{r}) \; + \; \beta(m + S(\mathbf{r})) \tag{2}$$

contains the average fields determined by the mesons, i.e. the attractive scalar field $S(\mathbf{r})$

$$S(\mathbf{r}) = g_\sigma \sigma(\mathbf{r}), \tag{3}$$

and the repulsive time-like component of the vector field $V_0(\mathbf{r})$

$$V_0(\mathbf{r}) = g_\omega \omega_0(\mathbf{r}) + g_\rho \tau_3 \rho_0(\mathbf{r}) + e\frac{1-\tau_3}{2} A_0(\mathbf{r}). \tag{4}$$

A magnetic potential $\boldsymbol{V}(\mathbf{r})$

$$\boldsymbol{V}(\mathbf{r}) = g_\omega \boldsymbol{\omega}(\mathbf{r}) + g_\rho \tau_3 \boldsymbol{\rho}(\mathbf{r}) + e\frac{1-\tau_3}{2} \boldsymbol{A}(\mathbf{r}), \tag{5}$$

originates from the space-like components of the vector mesons and behaves in the Dirac equation like a magnetic field. Therefore the effect produced by it is called *nuclear magnetism* [8].

Note that in these equations, the four-vector components of the vector fields ω^μ, ρ^μ, and A^μ are separated into the time-like (ω_0, ρ_0 and A_0) and space-like [$\boldsymbol{\omega} = (\omega^x, \omega^y, \omega^z)$, $\boldsymbol{\rho} = (\rho^x, \rho^y, \rho^z)$, and $\boldsymbol{A} = (A^x, A^y, A^z)$] components.

The cranked RHB-equations (1) contain three constraints characterized by three Lagrange parameters, the chemical potentials λ_τ ($\tau = n, p$) and the rotational frequency Ω_x. The chemical potentials λ_τ are determined by the average particle numbers for neutrons and protons ($\tau = n, p$)

$$\langle \Phi_\Omega | \hat{N}_n | \Phi_\Omega \rangle = N, \qquad \langle \Phi_\Omega | \hat{N}_p | \Phi_\Omega \rangle = Z. \tag{6}$$

The rotational frequency Ω_x along the x-axis is defined from the condition [12]

$$J_x(\Omega_x) = \langle \Phi_{\Omega_x} \mid \hat{J}_x \mid \Phi_{\Omega_x} \rangle = \sqrt{I(I+1)}. \tag{7}$$

where $J_x(\Omega_x)$ is the expectation value of the total angular momentum $\hat{\boldsymbol{J}}$ of the system along the x-axis and I is the total nuclear spin. The angular momentum is carried essentially by the fermions. As a result, the contributions of the meson fields to $J_x(\Omega_x)$ are neglected. The Coriolis term is given by

$$-\Omega_x \hat{J}_x = -\Omega_x \left(\hat{L}_x + \frac{1}{2}\hat{\Sigma}_x \right). \tag{8}$$

The time-independent inhomogeneous Klein-Gordon equations for the mesonic fields obtained by means of varia-

tional principle are given in the CRHB theory by [10, 11]

$$\begin{aligned}
\left\{-\Delta-(\Omega_x\hat{L}_x)^2+m_\sigma^2\right\}\ \sigma(\mathbf{r}) &= -g_\sigma\rho_s(\mathbf{r})-g_2\sigma^2(\mathbf{r})-g_3\sigma^3(\mathbf{r}),\\
\left\{-\Delta-(\Omega_x\hat{L}_x)^2+m_\omega^2\right\}\omega_0(\mathbf{r}) &= g_\omega\rho_v^{is}(\mathbf{r}),\\
\left\{-\Delta-[\Omega_x(\hat{L}_x+\hat{S}_x)]^2+m_\omega^2\right\}\ \boldsymbol{\omega}(\mathbf{r}) &= g_\omega\mathbf{j}^{is}(\mathbf{r}),\\
\left\{-\Delta-(\Omega_x\hat{L}_x)^2+m_\rho^2\right\}\rho_0(\mathbf{r}) &= g_\rho\rho_v^{iv}(\mathbf{r}),\\
\left\{-\Delta-[\Omega_x(\hat{L}_x+\hat{S}_x)]^2+m_\rho^2\right\}\ \boldsymbol{\rho}(\mathbf{r}) &= g_\rho\mathbf{j}^{iv}(\mathbf{r}),\\
-\Delta\ A_0(\mathbf{r}) = e\rho_v^p(\mathbf{r}), \qquad -\Delta\ \mathbf{A}(\mathbf{r}) &= e\mathbf{j}^p(\mathbf{r}),
\end{aligned} \tag{9}$$

where the source terms are sums of bilinear products of baryon amplitudes

$$\begin{aligned}
\rho_s(\mathbf{r}) &= \sum_{k>0}[V_k^n(\mathbf{r})]^\dagger\hat{\beta}V_k^n(\mathbf{r})+[V_k^p(\mathbf{r})]^\dagger\hat{\beta}V_k^p(\mathbf{r}),\\
\rho_v^{is}(\mathbf{r}) &= \sum_{k>0}[V_k^n(\mathbf{r})]^\dagger V_k^n(\mathbf{r})+[V_k^p(\mathbf{r})]^\dagger V_k^p(\mathbf{r}),\\
\rho_v^{iv}(\mathbf{r}) &= \sum_{k>0}[V_k^n(\mathbf{r})]^\dagger V_k^n(\mathbf{r})-[V_k^p(\mathbf{r})]^\dagger V_k^p(\mathbf{r}),\\
\mathbf{j}^{is}(\mathbf{r}) &= \sum_{k>0}[V_k^n(\mathbf{r})]^\dagger\hat{\boldsymbol{\alpha}}V_k^n(\mathbf{r})+[V_k^p(\mathbf{r})]^\dagger\hat{\boldsymbol{\alpha}}V_k^p(\mathbf{r}),\\
\mathbf{j}^{iv}(\mathbf{r}) &= \sum_{k>0}[V_k^n(\mathbf{r})]^\dagger\hat{\boldsymbol{\alpha}}V_k^n(\mathbf{r})-[V_k^p(\mathbf{r})]^\dagger\hat{\boldsymbol{\alpha}}V_k^p(\mathbf{r}).
\end{aligned} \tag{10}$$

The sums over $k>0$ run over all quasiparticle states corresponding to positive energy single-particle states (*no-sea approximation*) [13, 14]. In Eqs. (9,10), the indexes n and p indicate neutron and proton states, respectively, and the indexes *is* and *iv* are used for isoscalar and isovector quantities. $\rho_v^p(\mathbf{r})$, $\mathbf{j}^{\mathbf{p}}(\mathbf{r})$ in Eq. (9) correspond to $\rho_v^{is}(\mathbf{r})$ and $\mathbf{j}^{is}(\mathbf{r})$ defined in Eq. (10), respectively, but with the sums over neutron states neglected. $\hat{\boldsymbol{L}}=-i\mathbf{r}\times\boldsymbol{\nabla}$ is the orbital angular momentum operator of the scalar and the time-like meson fields and $\hat{\boldsymbol{L}}+\hat{\boldsymbol{S}}$ is the total angular momentum of the space-like parts of the vector fields. The operators $\hat{\mathbf{S}}$ are three 3×3 matrices representing the spin-matrices of vector fields (see [15]). Note that only x-components of these operators are considered in Eq. (10). The Coriolis terms $\Omega_x(\hat{L}_x+\hat{S}_x)$ and $\Omega_x\hat{L}_x$ can be neglected for reasons discussed in Sect. 8.1 of Ref. [1]. The Coriolis term for the Coulomb potential $A_0(\mathbf{r})$ and the spatial components of the vector potential $\mathbf{A}(\mathbf{r})$ are neglected in Eqs. (9) since the coupling constant of the electromagnetic interaction is small compared with the coupling constants of the meson fields.

Two terms in the Dirac equation, namely, the Coriolis operator $\hat{J}_x$ and the magnetic potential $\mathbf{V}(\mathbf{r})$ (as well as the currents $\mathbf{j}^{n,p}(\mathbf{r})$ in the Klein-Gordon equations) break time-reversal symmetry [17]. Their presence leads to the appearance of time-odd mean fields. However, one should distinguish time-odd mean fields originating from Coriolis operator and magnetic potential. The Coriolis operator is always present in the description of rotating nuclei in the framework of the cranking model. However, the cranked relativistic mean field (CRMF) calculations, with only these time-odd fields accounted for, underestimate the experimental moments of inertia [17–19]. A similar situation also holds in nonrelativistic theories [20, 21]. The inclusion of the currents $\mathbf{j}^{n,p}(\mathbf{r})$ into the Klein-Gordon equations, which leads to the space-like components of the vector ω and ρ mesons and thus to magnetic potential $\mathbf{V}(\mathbf{r})$, considerably improves the description of experimental moments of inertia.

Note that time-odd mean fields related to nuclear magnetism are defined through the Lorentz invariance [1, 16, 19] and thus they do not require additional coupling constants: the coupling constants of time-even mean fields are used also for time-odd mean fields. This is because the densities ρ and currents $\boldsymbol{j}$ (Eq. (10)) do not transform independently under Lorentz transformation since they form covariant four-vector $j^\mu=\{\rho,\mathbf{j}\}$. This fact explains why the structure of the Klein-Gordon equations for time-like and space-like components of vector mesons is the same (Eq. (10)) and why the same coupling constant stands in front of the densities and currents on the right hand side of these equations [16].

The currents are isoscalar and isovector in nature for the ω and ρ mesons (Eqs. (9 and 10)), respectively. As a consequence, the contribution of the ρ-meson to magnetic potential is marginal [16]. Thus, time-odd mean fields in the CDFT framework depend predominantly on the spatial components of the ω meson. Neglecting the contribution of the ρ meson, one can see that only two parameters, namely, the mass m_ω and coupling constant g_ω of the ω meson

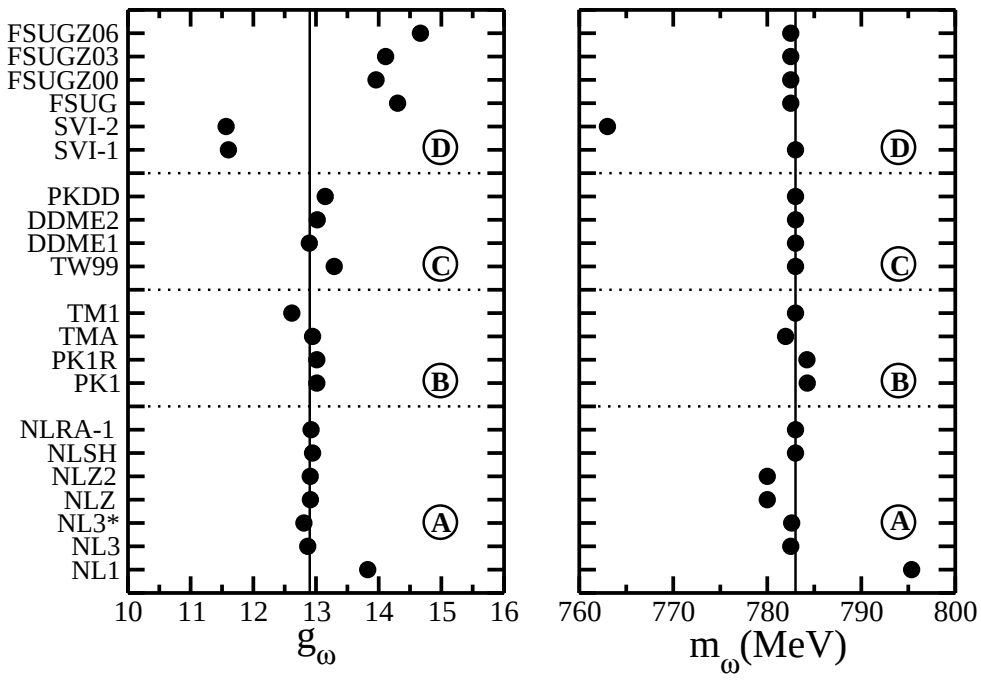

FIG. 1. The m_ω and g_ω parameters of different CEDF's. These CEDF's are combined into four groups dependent on how self- and mixed-couplings are introduced. Group A represents the CEDF's which include non-linear self-couplings only for the σ-meson. Group B contains the CEDF's which include self-couplings for the σ- and ω-mesons (and $\rho-$mesons in the case of PK1R). Group C represents the CEDF's which include density-dependent meson-nucleon couplings for the σ-, ω-, and ρ-mesons. The other CEDF's are included into the group D. For details see Ref. [16] from which this figure is taken.

define the properties of time-odd mean fields (Eqs. (5) and (9)). Fig. 1 clearly indicates that these parameters are well localized in the parameter space for the covariant energy density functionals (CEDF's) in the groups A, B, and C (Fig. 1). These are precisely the CEDF's which are extensively tested on nuclear structure data sensitive to time-even mean fields. For these CEDF's parameter dependence of the impact of time-odd mean fields on the physical observables is quite weak [16, 19, 22]. This parameter dependence is expected to be larger in group D. However, at present it is not clear whether the CEDF's in this group are reasonable ones since they have not been tested on nuclear structure data.

Time-odd mean fields appear only in nuclear systems with broken time-reversal symmetry. They affect magnetic moments [23], isoscalar monopole vibrations [24], electric giant resonances [25], large amplitude collective dynamics [26], fussion process [27], the strengths and energies of Gamow-Teller resonances [28], the binding energies of odd-mass nuclei [29–31] and the definition of the strength of pairing correlations [16, 31, 32]. However, as discussed in detail in Sect. III they are especially pronounced in rotating nuclei.

The pairing potential (field) $\hat{\Delta}$ in Eq. (1) is given by

$$\hat{\Delta} \equiv \Delta_{ab} \;=\; \frac{1}{2}\sum_{cd} V^{pp}_{abcd}\kappa_{cd} \tag{11}$$

where the indices $a, b, \ldots$ denote quantum numbers which specify the single-particle states with the space coordinates $\mathbf{r}$ as well as the Dirac and isospin indices s and τ. It contains the pairing tensor κ [2]

$$\kappa = V^* U^T \tag{12}$$

and the matrix elements V^{pp}_{abcd} of the effective interaction in the pp-channel. The phenomenological Gogny D1S finite range interaction [33] is used as such effective interaction in all CRHB calculations. It is given by

$$V^{pp}(1,2) = f\sum_{i=1,2} e^{-[(\mathbf{r}_1-\mathbf{r}_2)/\mu_i]^2}\times(W_i + B_i P^\sigma - H_i P^\tau - M_i P^\sigma P^\tau) \tag{13}$$

[2] This quantity is sometimes called as *abnormal density*.

where μ_i, W_i, B_i, H_i and M_i $(i = 1, 2)$ are the parameters of the force and P^σ and P^τ are the exchange operators for the spin and isospin variables, respectively. This interaction is density-independent. Note also that an additional factor f affecting the strength of the Gogny force is introduced in Eq. (13) (see Refs. [31, 34, 35] for the reasons of its introduction).

In the CRHB calculations, the size of the pairing correlations is measured in terms of the pairing energy defined as

$$E_{pairing} = -\frac{1}{2}\mathrm{Tr}(\Delta\kappa). \tag{14}$$

Note that this is not an experimentally accessible quantity.

One should note that the Bogoliubov transformation is not commutable with the nucleon number operator and consequently the resulting wave function does not correspond to a system having a definite number of protons and neutrons. The best way to deal with this problem would be to perform an exact particle number projection before the variation [36]; however, such calculations are expected to be extremely time-consuming for realistic interactions. As a result, an approximate particle number projection by means of the Lipkin-Nogami (LN) method [37–40] is used in the CRHB calculations because of its simplicity. The details of the implementation of this method into the CRHB framework are given in Ref. [11]; the CRHB calculations with the LN method included are abbreviated as CRHB+LN ones. The application of the LN method considerably improves an agreement with experiment for rotational properties (see Refs. [11, 41, 42]).

The total energy of system in the laboratory frame is given as a sum of fermionic (E^{F}) and bosonic (E^{B}) contributions

$$E_{\mathrm{CRHB}} = E^{\mathrm{F}} + E^{\mathrm{B}}. \tag{15}$$

The fermionic energies E^{F} are given by

$$E^{\mathrm{F}} = E_{part} + \Omega_x J + E_{pairing} + E_{cm} \tag{16}$$

where

$$E_{part} = Tr(h_D\rho), \qquad J = Tr(j_x\rho), \tag{17}$$

are the particle energy and the expectation value of the total angular momentum along the rotational axis and E_{cm} is the correction for the spurious center-of-mass motion.

The bosonic energies E^{B} in the laboratory frame are given by

$$\begin{aligned} E^{\mathrm{B}} =& -\frac{1}{2}\int d\mathbf{r}\,[g_\sigma\,\sigma(\mathbf{r})\rho_s(\mathbf{r}) + \frac{1}{3}g_2\sigma^3(\mathbf{r}) + \frac{1}{2}g_3\sigma^4(\mathbf{r})] \\ & -\frac{1}{2}\,g_\omega\int d\mathbf{r}\,[\omega_0(\mathbf{r})\rho_v^{is}(\mathbf{r}) - \boldsymbol{\omega}(\mathbf{r})\mathbf{j}^{is}(\mathbf{r})] \\ & -\frac{1}{2}\,g_\rho\int d\mathbf{r}\,[\rho_0(\mathbf{r})\rho_v^{iv}(\mathbf{r}) - \boldsymbol{\rho}(\mathbf{r})\mathbf{j}^{iv}(\mathbf{r})] \\ & -\frac{1}{2}\,e\int d\mathbf{r}\,[A_0(\mathbf{r})\rho_v^{p}(\mathbf{r}) + \boldsymbol{A}(\mathbf{r})\mathbf{j}^{p}(\mathbf{r})] \\ & +\Omega_x^2\int d\mathbf{r}\,[\sigma(\mathbf{r})\hat{L}_x^2\sigma(\mathbf{r}) - \omega_0(\mathbf{r})\hat{L}_x^2\omega_0(\mathbf{r}) + \boldsymbol{\omega}(\mathbf{r})(\hat{L}_x+\hat{S}_x)^2\boldsymbol{\omega}(\mathbf{r}) \\ & \qquad -\rho_0(\mathbf{r})\hat{L}_x^2\rho_0(\mathbf{r}) + \boldsymbol{\rho}(\mathbf{r})(\hat{L}_x+\hat{S}_x)^2\boldsymbol{\rho}(\mathbf{r})] \end{aligned} \tag{18}$$

Cranked relativistic mean field (CRMF) theory is a limiting case of the CRHB theory in which the pairing correlations are neglected; the details of the formalism can be found in Refs. [8, 18, 43]. It has been an important step in the development of the CDFT theory to the description of rotating nuclei and, as exemplified in the present paper, still remains a powerfull theoretical tool for the studies of rotating nuclei in unpaired regime at high spin.

III. TIME-ODD MEAN FIELDS IN ROTATING NUCLEI

Nuclear magnetism, i.e. the time-odd component of the mean fields $\boldsymbol{V}(\mathbf{r})$, appears only in nuclear systems with broken time-reversal symmetry in the intrinsic frame. Rotating nuclei represent a system which is strongly affected by time-odd mean fields. In rotating nuclei, the average field has two sources of time-reversal symmetry breaking, the Coriolis operator $\Omega\hat{J}_x$ and the magnetic part of the vector fields $\boldsymbol{V}(\mathbf{r})$(Eq. (5)) induced in a self-consistent way by the

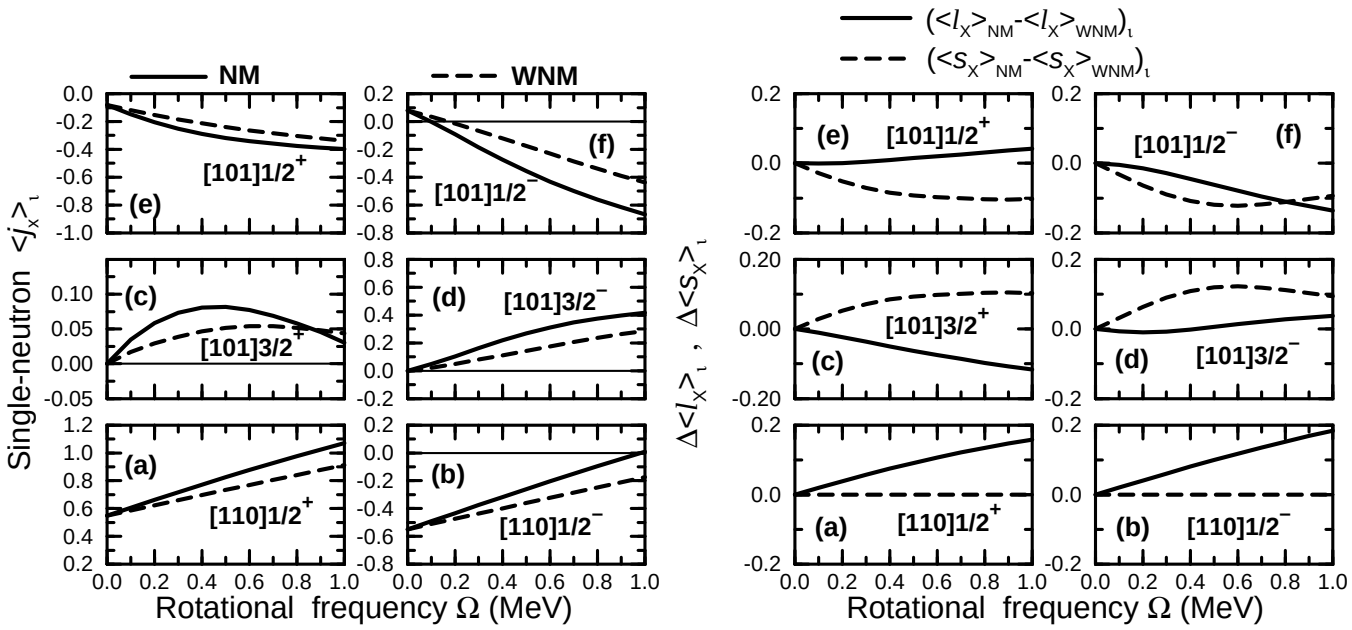

FIG. 2. Left two columns: expectation values $\langle\hat{j}_x\rangle_i$ of the neutron orbitals forming the $N = 1$ shell calculated with and without nuclear magnetism. The orbitals are labeled by the Nilsson quantum numbers $[Nn_z\Lambda]\Omega$ and the sign of the signature $r = \pm i$. Right two columns: the changes of the expectation values of spin and orbital angular momenta caused by nuclear magnetism. The results presented are from the study of doubly magic superdeformed configuration in ^{152}Dy. From Ref. [17].

currents. In this section, the results obtained with and without nuclear magnetism are denoted as NM and WNM, respectively.

The physical observables, most frequently used in the analysis of rotating nuclei, are kinematic ($J^{(1)}$) and dynamic ($J^{(2)}$) moments of inertia which are defined as

$$J^{(1)}(\Omega_x) = \frac{J}{\Omega_x}, \qquad J^{(2)}(\Omega_x) = \frac{dJ}{d\Omega_x} \tag{19}$$

where J is the expectation value of the total angular momentum along the x-axis. In the CRMF theory, this quantity is defined as a sum of the expectation values of the single-particle angular momentum operators $\hat{j}_x$ of the occupied states

$$J = \sum_i \langle i|\hat{j}_x|i\rangle. \tag{20}$$

Thus, the modifications of the moments of inertia due to NM, which as discussed below are important in rotating nuclei, can be traced back to the changes of the single-particle expectation values $\langle\hat{j}_x\rangle_i = \langle i|\hat{j}_x|i\rangle$ and the corresponding contributions of spin ($\langle\hat{s}_x\rangle_i$) and orbital ($\langle\hat{l}_x\rangle_i$) angular momenta [17].

On the microscopic level, the contribution to $\langle\hat{j}_x\rangle_i$ due to NM is defined as [17]

$$\Delta\langle j_x\rangle_i = \langle\hat{j}_x\rangle_i^{NM} - \langle\hat{j}_x\rangle_i^{WNM}. \tag{21}$$

Fig. 2 shows that the $\Delta\langle j_x\rangle_i$ is positive at the bottom and negative at the top of the N-shell [17]. The absolute value of $\Delta\langle j_x\rangle_i$ correlates with the absolute value of $\langle\hat{j}_x\rangle_i$. Note that the contributions to $\langle\hat{j}_x\rangle_i$ due to NM are small in the middle of the shell. The $\Delta\langle j_x\rangle_i$ contributions can be decomposed into the contributions due to spin ($\Delta\langle s_x\rangle_i$) and orbital ($\Delta\langle l_x\rangle_i$) angular momenta using equations similar to Eq. 21. As shown in right panels of Fig. 2 these contributions have complicated dependences both on the frequency and the structure of the single-particle orbital under study [17].

Oscillator shells with higher N-values show a similar behavior. At a given rotational frequency the modifications of single-particle $\langle\hat{j}_x\rangle_i$ values induced by NM lead to an increase of the total J and of the moments of inertia (see Figs. 3 and 5 below). This means that NM enhances the angular momentum in rotating nuclei in addition to the Coriolis term.

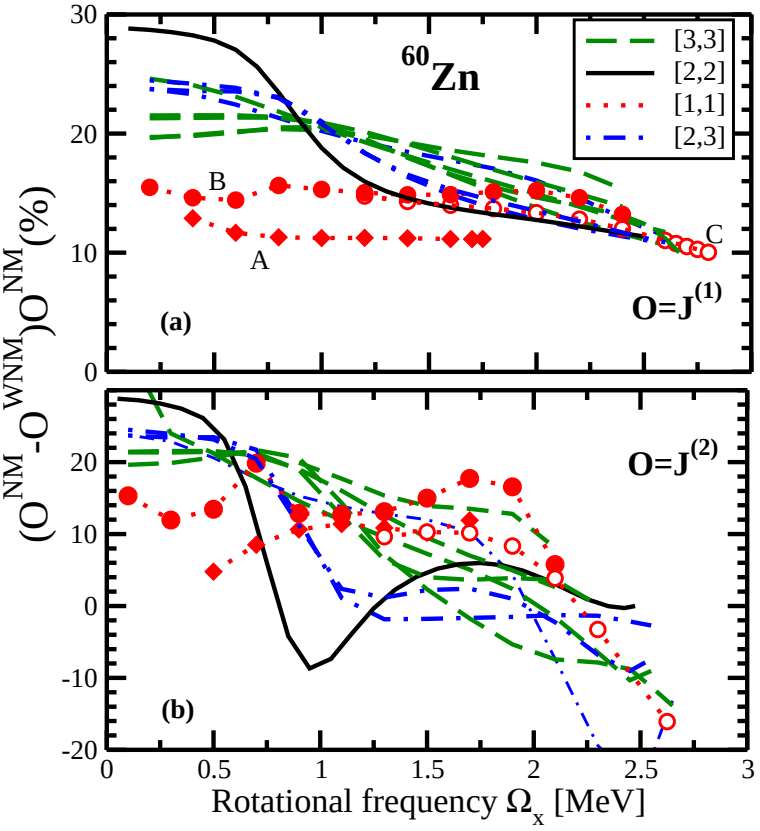

FIG. 3. The contributions of NM to the dynamic ($J^{(2)}$) (panel (b)) and kinematic ($J^{(1)}$) (panel (a)) moments of inertia as a function of rotational frequency for highly-deformed and superdeformed configurations of ^{60}Zn obtained in the CRMF calculations. Different color/line types are used for different groups of configurations. notation $[n, p]$, where $n(p)$ is the number of occupied $g_{9/2}$ neutrons (protons). From Ref. [19].

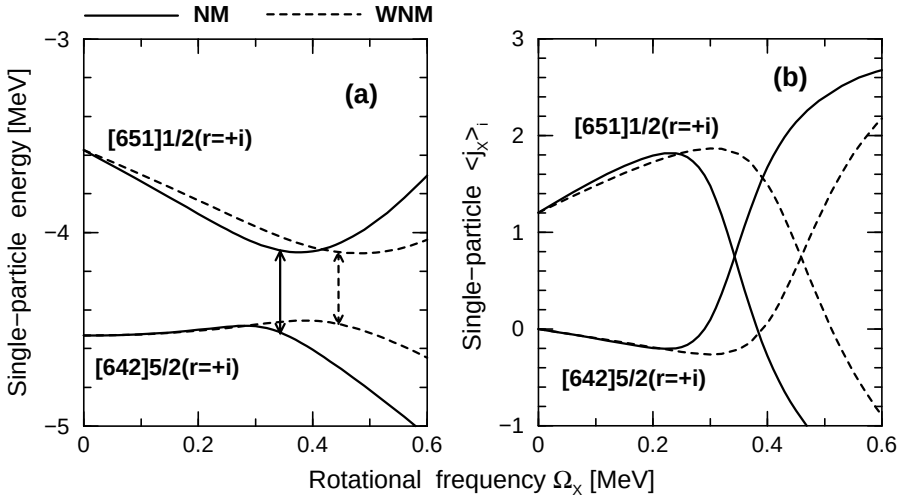

FIG. 4. (a) Proton single-particle energies (Routhians) in the self-consistent rotating potential as a function of rotational frequency Ω_x obtained in the CRMF calculations with and without NM. They are given along the deformation path of the lowest SD configuration in ^{194}Pb. Only interacting $[651]1/2^+$ and $[642]5/2^+$ orbitals are shown, see Fig. 1 in Ref. [11] for full spectra. (b) The expectation values $\langle\hat{j}_x\rangle_i$ of the single-particle angular momentum operator $\hat{j}_x$ of the orbitals shown on panel (a). Solid and dashed arrows are used to indicate the frequencies (as well as the energy gap between the interacting orbitals in panel (a)) at which the band crossings take place in the calculations with and without NM, respectively. From Ref. [19].

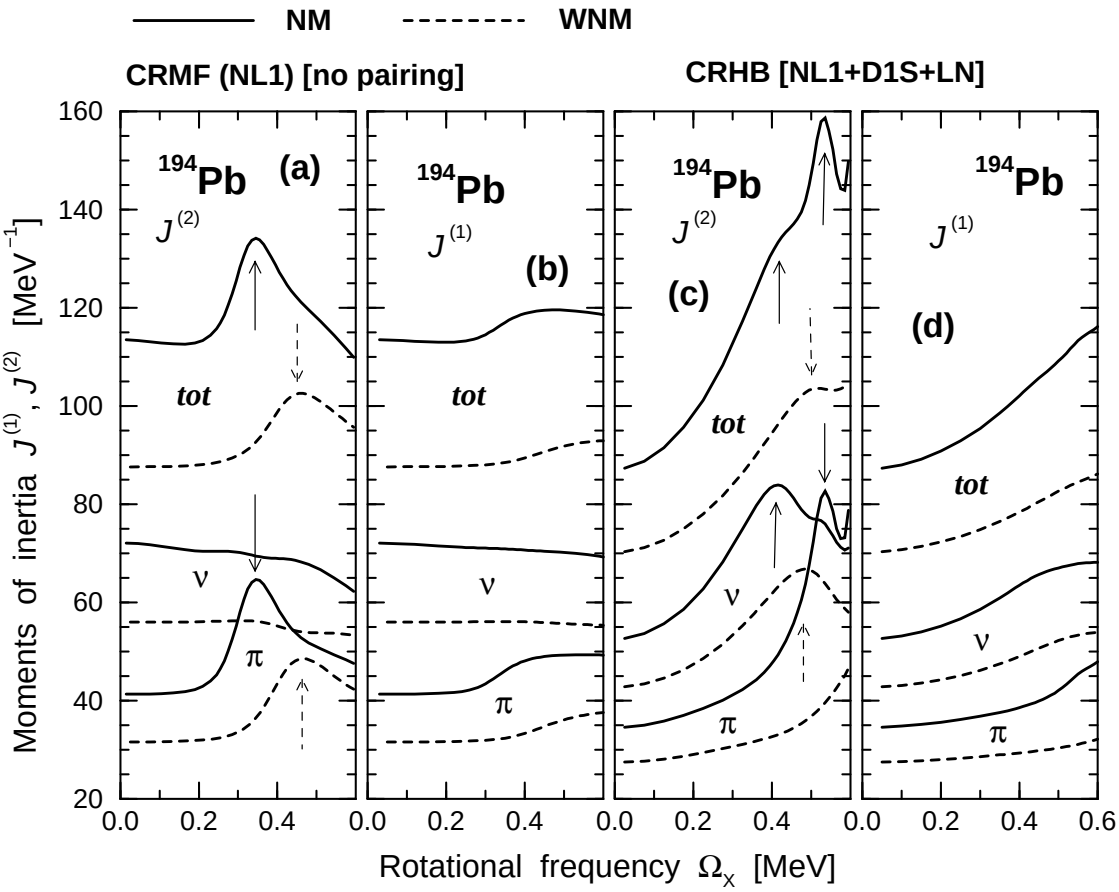

FIG. 5. Kinematic ($J^{(1)}$) and dynamic ($J^{(2)}$) moments of inertia for the lowest SD configuration in ^{194}Pb obtained in the calculations with and without NM. Proton and neutron contributions to these quantities are indicated by π and ν, while total moments by '*tot*'. Panels (a) and (b) show the results obtained in the calculations without pairing, while panels (c) and (d) show the results of the calculations within the CRHB+LN framework. Solid and dashed arrows are used to indicate the frequencies at which the band crossings take place in the calculations with and without NM, respectively. From Ref. [19].

The most important impact of NM on physical observables is revealed in the moments of inertia. To quantify this impact, the contribution $\Delta O^{NM-contr}$ (in percentage) of NM to the physical observable O is defined as

$$\Delta O^{NM-contr} = \frac{O^{NM} - O^{WNM}}{O^{NM}} \times 100\%. \tag{22}$$

The increase of the moments of inertia due to NM has been studied first in a semiclassical approximation in Ref. [44], then in fully self-consistent CRMF calculations on the example of the yrast SD band in ^{152}Dy in Ref. [18] and finally in a systematic way in Refs. [17, 19, 22]. NM typically increases the calculated kinematic moments of inertia of normal-deformed rotational bands in the rare-earth region by 10-30% [19]. Considerable fluctuations of the $(J^{(1)}_{NM} - J^{(1)}_{WNM})/J^{(1)}_{NM}$ quantity as a function of proton and neutron numbers seen in some isotonic and isotopic chains at normal deformation are due to the changes in underlying single-particle structure. The $(J^{(1)}_{NM} - J^{(1)}_{WNM})/J^{(1)}_{NM}$ quantity is around 20% in the superdeformed bands of the $A \sim 150$ mass region and around 20-25% in the hyperdeformed bands in the $Z = 40 - 58$ part of nuclear chart at typical frequencies at which these bands are either observed or expected to be observed.

The configuration and frequency dependence of the impact of NM on the moments of inertia is shown in Fig. 3a. With increasing rotational frequency, the average contribution of NM into kinematic moments of inertia decreases and it falls below 15% at $\Omega_x \sim 2.5$ MeV . In addition, the configuration dependence of the $\Delta J^{(1)}_{NM-contr}$ quantities is weaker than the one at low frequencies. At these frequencies, the majority of occupied single-particle orbitals are either completely aligned or very close to complete alignment. However, NM do not modify the expectation values of the single-particle angular momenta $\langle j_x \rangle_i$ of completely aligned orbitals [22]. As a result, only remaining orbitals,

which are still aligning, contribute into $\Delta J^{(1)}_{NM-contr}$. The combined contribution of these orbitals into $\Delta J^{(1)}_{NM-contr}$ is smaller than the one at lower frequencies because the alignment of these orbitals is not far away from complete. The impact of NM on the dynamic moments of inertia is shown in Fig. 3b and it clearly displays much more complicated pattern as compared with the impact of NM on the kinematic moments of inertia (see Ref. [19] for details).

The modification of the single-particle alignments and energies in the presence of NM leads to substantial impact on the band crossing properties. This is illustrated in Figs. 4 and 5 on the example of the lowest superdeformed (SD) band in ^{194}Pb.

In the CRMF calculations, the unpaired proton band crossing originates from the interaction between the $\pi[642]5/2^+$ and $\pi[651]1/2^+$ orbitals (Fig. 4a). Since NM increases somewhat the single-particle alignment $\langle \hat{j}_x \rangle_i$ (Fig. 4b) and the slope of the routhian for the $\pi[651]1/2^+$ orbital (Fig. 4a), the band crossing takes place at lower frequency. The shift of crossing frequency due to NM is considerable (120 keV) from 0.465 MeV (WNM) down to 0.345 MeV (NM), Fig. 4a. The calculations also suggest that the strength of the interaction between two interacting orbitals at the band crossing is modified in the presence of NM as seen in the change of the energy distance (gap) between these two orbitals at the crossing frequency (Fig. 4a).

The impact of NM on band crossing features is also seen in the CRHB+LN calculations where the alignment of the pairs of $j_{15/2}$ neutrons and $i_{13/2}$ protons causes the shoulder and peak in total dynamic moment of inertia $J^{(2)}$ (Fig. 5c) (see also Ref. [11]). Note that each of these two alignments creates a peak in the dynamic moment of inertia of corresponding subsystem. NM shifts the paired neutron band crossing to lower frequencies by 70 keV from 0.485 MeV (WNM) to 0.415 MeV (NM). Paired proton band crossing lies in the calculations with NM at $\Omega_x = 0.535$ MeV, while only the beginning of this crossing is seen in the calculations without NM (Fig. 5c).

The origin of this effect is twofold. Similar to the unpaired calculations, the part of it can be traced to the fact that NM increases the expectation values $\langle \hat{j}_x \rangle_i$ of the orbitals located at the bottom of the shell (the discussed orbitals are of this kind) [17]. The corresponding larger slope of the quasiparticle routhians causes the shift of the crossing to lower frequencies.

However, an additional contribution comes from the modification of the pairing by NM. There is a difference in the pairing energies calculated with and without NM which increases with rotational frequency, see Fig. 3c in Ref. [19]. The pairing in the calculations with NM is weaker. This can be explained by the increase of $\langle \hat{j}_x \rangle_i$ of the orbitals located at the bottom of the shell due to NM (see above). Thus in the presence of NM the gradual breaking of high-j pairs proceeds faster which leads to a faster reduction of pairing with increasing Ω_x as compared with the WNM calculations. This effect is called as *an anti-pairing effect induced by NM* [19].

Above discussed CRMF and CRHB+LN examples clearly show that the modifications of band crossing features (crossing frequencies and the features of the kinematic and dynamic moments of inertia in band crossing region) caused by NM are substantial and depend on the underlying modifications of single-particle properties such as alignments and single-particle (quasi-particle) energies.

The changes of single-particle properties induced by nuclear magnetism affect also other physical observables in rotating nuclei, the discussion of which is not possible due to space limitations. These are

- *modifications of the energy splittings between signature partner orbitals (signature splitting)* [17]. These modifications represent an additional source of band crossing frequency changes in odd- and odd-odd nuclei and excited configurations of even-even ones in the presence of NM (Sect. III in Ref. [19].

- *modifications of the effective alignments i_{eff} [17].* This observable is often used in the analysis of the single-particle structure of superdeformed bands (see Ref. [45])

- *the existence of signature-separated rotational bands.* [19, 46, 47]. They reveal themselves in a considerable energy splitting of the $r_{tot} = +1$ and $r_{tot} = -1$ branches of the configurations which have the same structure in terms of occupation of single-particle states with given Nilsson labels. *This feature is a strong spectroscopic fingerprint of the presence of time-odd mean fields.*

- *Within specific configuration the impact of NM on the binding energies reaches its maximum at the terminating state [22].* Underlying microscopic mechanism for additional binding due to NM at such states has the same features as those seen in low-spin one- and two-particle configurations of odd and odd-odd nuclei [16]. However, the magnitude of the effects is significantly larger.

- The values of kinematic moment of inertia calculated with NM are typically within 5% of the rigid body value for the moments of inertia at super- and hyperdeformation [19], but the deviations from the rigid-body value are significantly larger for normal-deformed bands.

- NM has very small effect on the deformation properties of nuclei [16, 17, 19].

IV. CURRENTS IN THE INTRINSIC (ROTATING) FRAME

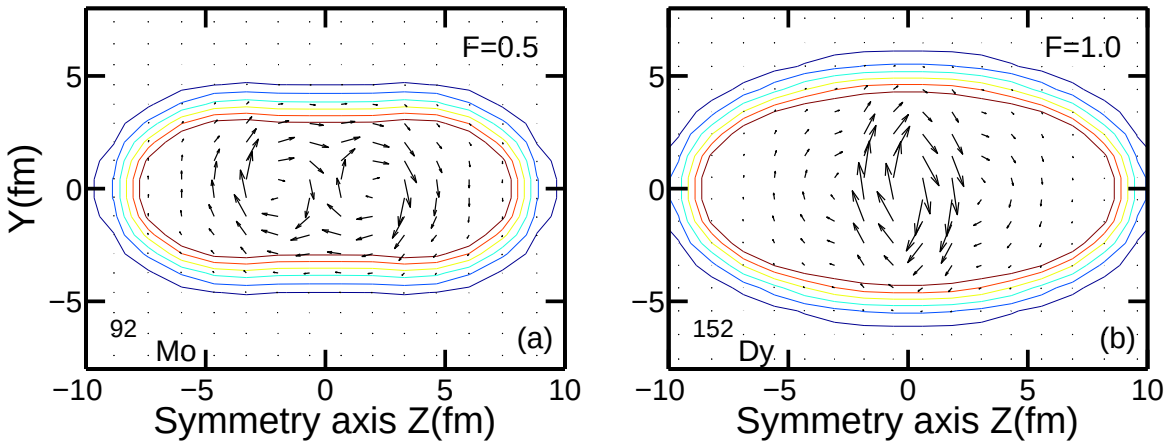

FIG. 6. Total neutron current distributions $\mathbf{j}^n(\mathbf{r})$ in the intrinsic frame in the $y-z$ plane for the yrast hyperdeformed (^{92}Mo) and superdeformed (^{152}Dy) configurations at rotational frequencies $\Omega_x \sim 1.0$ MeV and $\Omega_x = 0.5$ MeV, respectively. The currents in panel (b) are plotted at arbitrary units for better visualization. The currents in panel (a) are normalized to the currents in panel (b) by using factor F. The shape and size of the nucleus are indicated by density lines which are plotted in the range $0.01 - 0.06$ fm^{-3} in step of 0.01 fm^{-3}. Based on Fig. 8 of Ref. [19].

The Coriolis term is present in NM and WNM calculations. This means that the currents (Eq. (10)) are always present in rotating nuclei. However, it is important to distinguish the currents induced by the Coriolis term and the ones which appear due to magnetic potential. The currents, which appear in the WNM calculations, are generated by the Coriolis term. Thus, following Ref. [19] they are called as *Coriolis induced currents*. On the contrary, the currents in the NM calculations are generated by both the Coriolis term and magnetic potential. The difference of the currents in the NM and WNM calculations is attributable to magnetic potential. Thus, the currents $[\mathbf{j}^{n,p}(\mathbf{r})]^{NM} - [\mathbf{j}^{n,p}(\mathbf{r})]^{WNM}$ are called as *magnetic potential induced currents* [19].

The detailed analysis of the currents in the rotating nuclei in the CDFT framework has first been performed in Ref. [19] [3] The currents in the rotating frame of reference that is fixed to the body is caused by quantized motion of the fermions. Complicated structure of the currents in the rotating systems of independent fermions visible in Fig. 6 is the consequence of the fact that total current is the sum of the single-particle currents. The single-particle currents show vortices (circulations), the existence of which implies non-vanishing current circulations defined as $\mathbf{C}(\mathbf{r}) = \nabla \times \mathbf{j}(\mathbf{r})$ [54]. Note that the strength and localization of vortices depends on the single-particle state (see Fig. 7). As a result, the differences seen in total currents of different nuclei/structures in Fig. 6 can be traced back to the single-particle content of underlying single-particle configuration.

The localization, the strength and the structure of the current vortices created by a particle in a specific single-particle state depend on its nodal structure (see Ref. [54] and Sec. IIIC in Ref. [16]). In a slowly rotating anisotropic harmonic oscillator potential Coriolis induced current for a single particle shows a rather simple structure with the centers of the circulations found at the nodes and peaks of the oscillator eigenfunctions [54]; this structure forms a rectangular array somewhat similar to a crystal lattice. The analysis of single-particle vortices in rotating nuclei in the CRMF framework in general confirms these results (see Fig. 7 and Ref. [19]). In part, this is due to the fact that magnetic potential induced currents are weaker than Coriolis induced ones.

The typical features of the single-particle currents in the CRMF approach are seen in Fig. 7. The comparison of left and right columns of this figure clearly indicates that for a given single-particle state the increase of rotational frequency (i) does not lead to appreciable modifications of the density distribution but (ii) considerably modifies the strength of the currents and changes the shape of circulations. The latter is due to two factors. First, the Coriolis induced currents become active at $\Omega_x \neq 0.0$ MeV and at $\Omega_x = 0.5$ they are dominant type of currents. Second, the wave function undergoes considerable modifications with increasing rotational frequency. For example, the wave function (in terms of two largest components) of the $\nu[770]1/2^-$ state changes from 62%[770]1/2+17%[761]1/2 at $\Omega_x = 0.0$ MeV to 39%[770]1/2+28%[761]3/2 and $\Omega_x = 0.5$ MeV.

[3] For earlier studies of the currents in rotating nuclei in non-relativistic frameworks see Refs. [48–56].

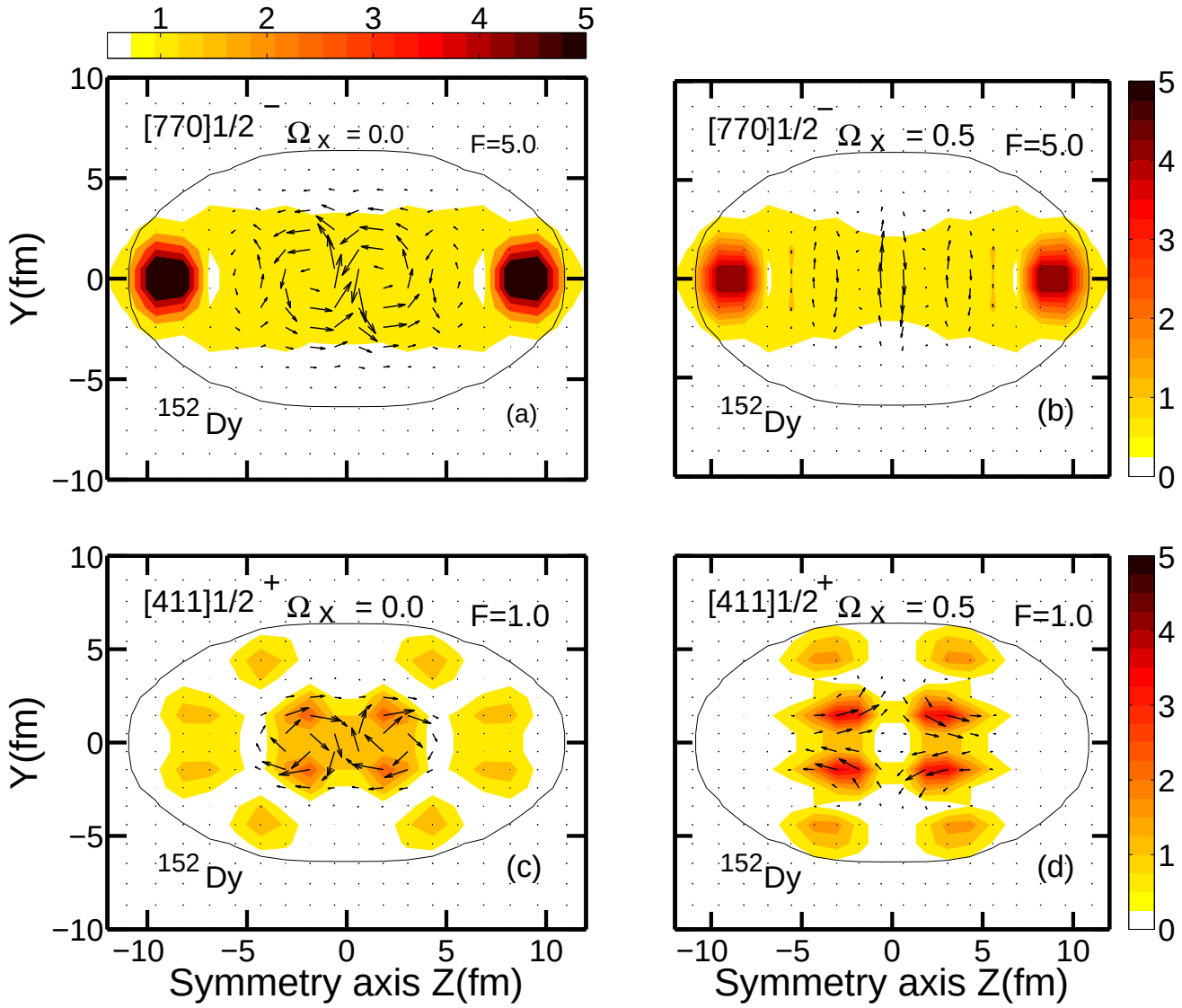

FIG. 7. Current distributions $\mathbf{j}^n(\mathbf{r})$ produced by single neutron in indicated single-particle states of the yrast SD configuration in ^{152}Dy at rotational frequencies $\Omega_x = 0.0$ MeV (left panels) and $\Omega_x = 0.5$ MeV (right panels). The shape and size of the nucleus are indicated by density line which is plotted at $\rho = 0.01$ fm^{-3}. The currents in panels (c) and (d) are plotted at arbitrary units for better visualization. The currents in panels (a) and (b) are normalized to the currents in panels (c) and (d) by using factor F. The currents and densities are shown in the intrinsic frame in the $y - z$ plane at $x = 0.48$ fm. The single-neutron density distributions due to the occupation of the indicated Nilsson state are shown by colormap. Note that slightly different colormap is used in panel (a) for better visualization of densities. Based on Fig. 9 of Ref. [19].

The total current is the sum of Coriolis induced and magnetic potential induced currents. In the majority of the cases total current is dominated by the Coriolis induced currents; magnetic potential induced currents represent approximately 5-20% [30%] of total current in the HD and SD [ND] nuclei [19]. The spatial distribution of Coriolis induced and magnetic potential induced currents is similar in the majority of nuclei. However, there are cases in which the spatial distribution of these two types of currents differ substantially [19]. Note that current is weak in the surface area (Fig. 6). This is contrary to semiclassical description of currents in normal and superfluid rotating nuclei [49] according to which the average intrinsic current flows mainly in the nuclear surface area. This underlines the importance of quantum mechanical treatment of the currents.

It is well known that there are no currents in the intrinsic frame if the rigid non-spherical body rotates uniformly (rigid rotation) (see Sec. 6A-5 in Ref. [57]). The moments of inertia of super- and hyperdeformed configurations in unpaired regime come very close to the rigid-body values in the CRMF calculations [19]. However, the intrinsic currents display the dramatic deviations from rigid rotation (Fig. 6). This clearly shows that the closeness of the

moments of inertia to rigid body value does not necessary implies that the current distribution should correspond to rigid rotation. On a microscopic level, the building blocks of the total current, namely, the single-particle currents certainly do not have a rigid-flow character; on the contrary, they have the vortex-flow character (see Fig. 7).

V. GROUND STATE ROTATIONAL BANDS IN NORMAL-DEFORMED EVEN-EVEN NUCLEI

Despite considerable amount of experimental data on normal-deformed nuclei and the availability of relevant theoretical frameworks, only recently and only in a single region (actinides) of nuclear chart the systematic investigation of rotational properties has been performed in the DFT framework. These are the studies of Refs. [42, 58] performed in the CDFT framework. On the contrary, only few nuclei have been studied at normal deformation in non-relativistic DFT [59–63]. In the current section I will review the major features of the rotational bands in the actinides and assess the accuracy of the description of these bands in the CRHB+LN framework.

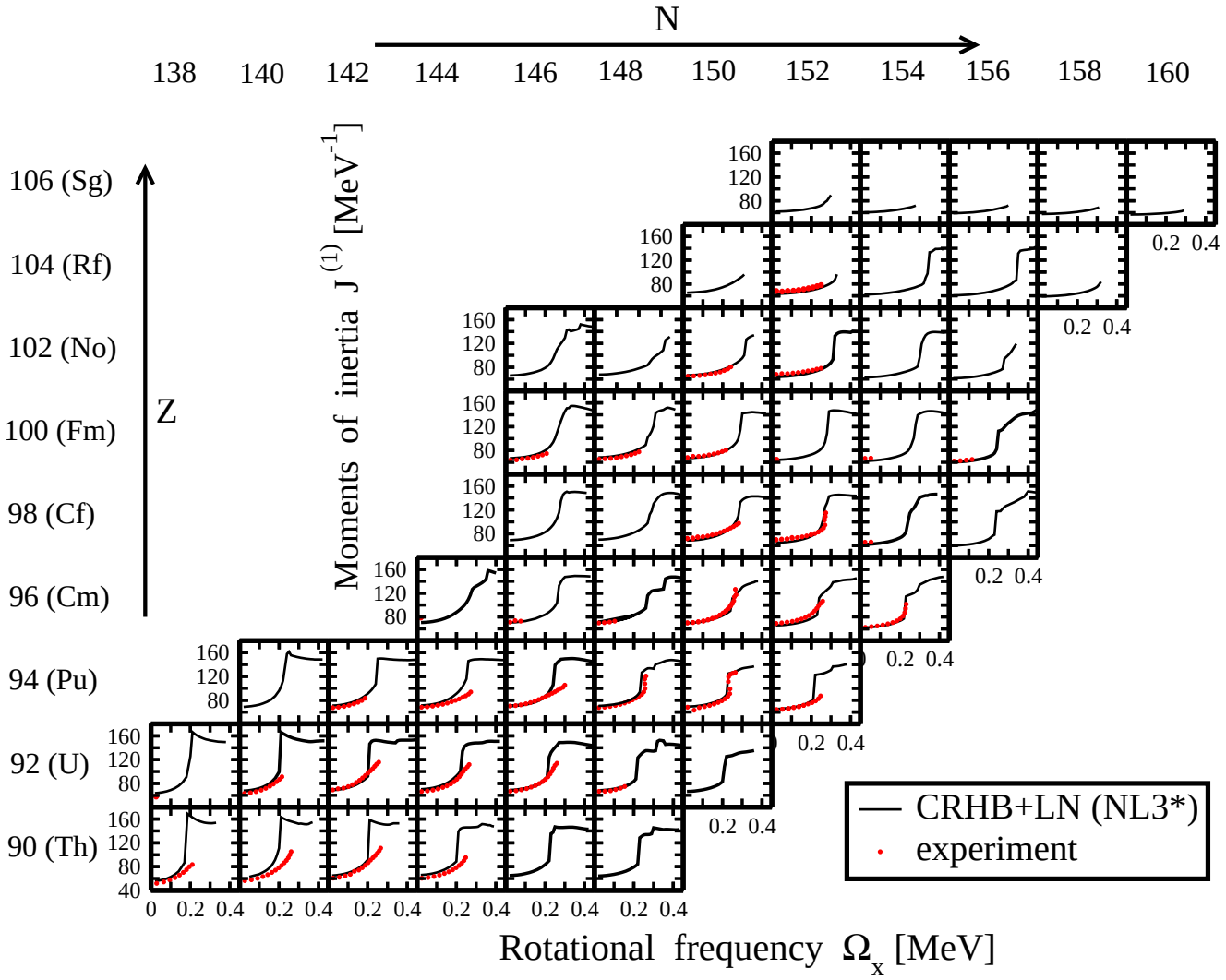

FIG. 8. The experimental and calculated moments of inertia $J^{(1)}$ as a function of rotational frequency Ω_x. The calculations are performed with the NL3* CEDF [64]. Calculated results and experimental data are shown by black lines and red dots, respectively. Cyan dots show new experimental data from Ref. [65] which were not included in Ref. [42]. From Refs. [42, 58].

Fig. 8 shows the results of the first ever (in any DFT framework) systematic investigation of rotational properties of even-even nuclei at normal deformation [42]. The calculations are performed within the CRHB+LN approach [11]. One can see that the gradual increases of the moments of inertia below band crossings are reproduced well. The upbendings observed in a number of rotational bands of the $A \geq 242$ nuclei are also reasonably well described in model calculations. However, the calculations also predict similar upbendings in lighter nuclei, but they have

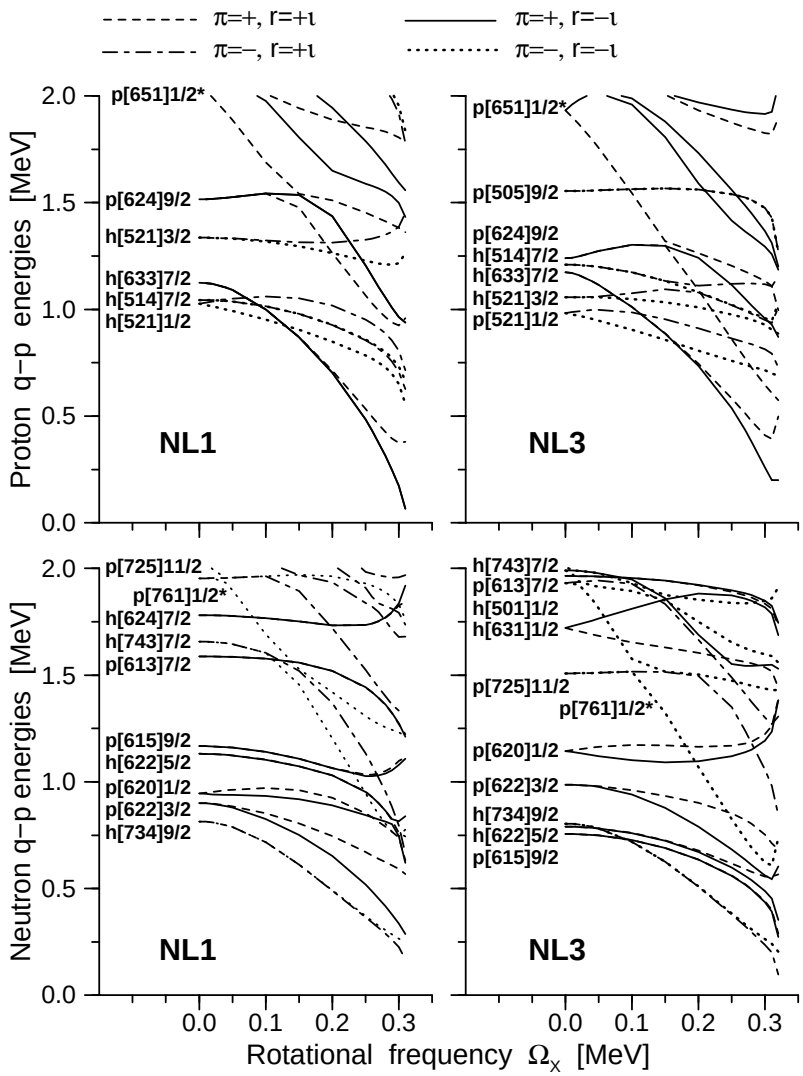

FIG. 9. Proton (top panels) and neutron (bottom panels) quasiparticle energies corresponding to the lowest configuration in ^{254}No. The CRHB+LN calculations have been performed with the NL1 (left panels) and NL3 (right panels) parametrizations. The letters 'p' and 'h' before the Nilsson labels are used to indicate whether a given routhian is of particle or hole type. From Ref. [31].

not been seen in experiment. Note that similar problems exist also in the cranking model calculations based on phenomenological potentials [42]. The analysis of Ref. [42] suggests that the stabilization of octupole deformation at high spin, not included in the present CRHB+LN calculations, could be responsible for this discrepancy between theory and experiment.

Either sharp or more gradual increases of the kinematic moments of inertia are observed at $\Omega_x \approx 0.2 - 0.30$ MeV (Fig. 8). They are due to the alignments of the neutron $j_{15/2}$ and proton $i_{13/2}$ orbitals which in many cases take place at similar rotational frequencies. The situation is more complicated than in the rare-earth region in which the $h_{11/2}$ protons align substantially later than the $i_{13/2}$ neutrons. For example, the routhian diagrams (Fig. 9) show simultaneous alignment of the proton $i_{13/2}$ pair ($\pi[633]7/2$ Nilsson orbit) and neutron $j_{15/2}$ pair ($\nu[734]9/2$ orbit) at $\Omega_x \approx 0.32$ MeV in ^{254}No. In the calculations with NL3 CEDF, the total angular momentum gain at the band crossing is $\approx 17\hbar$, with proton and neutron contributions of $\approx 7\hbar$ and $\approx 10\hbar$, respectively [31]. The alignment of these orbitals leads to a decrease of the mass hexadecapole moment Q_0, to a sign change of the mass hexadecapole moment Q_{40} and to an appreciable increase of the absolute value of the γ-deformation (Fig. 10a,b and c); this type of behavior is typical for the bands in this mass region. In addition, the pairing energies decrease with increasing rotational frequency due to the Coriolis anti-pairing effect and the pairing becomes very weak above the band crossing region (Fig. 10d).

Fig. 11 illustrates the accuracy of the description of band crossing features in the Pu and Cm nuclei. Here I will

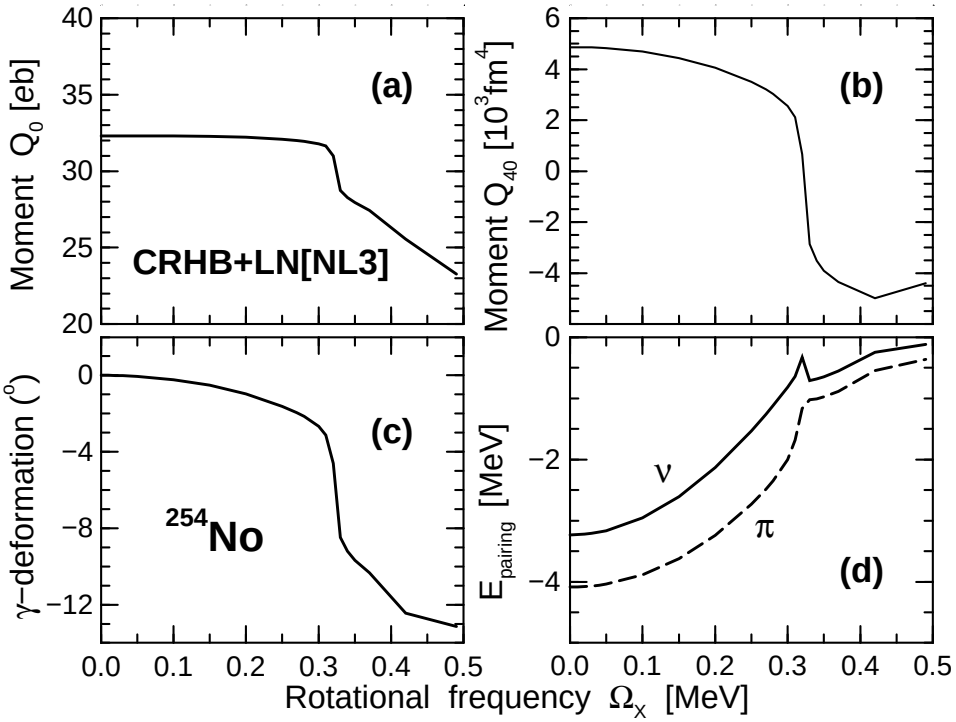

FIG. 10. Calculated mass quadrupole (Q_0) and hexadecapole (Q_{40}) moments, the γ-deformation and proton and neutron pairing energies ($E_{pairing}$) of the ground state rotational band in ^{254}No as a function of rotational frequency Ω_x. The results are obtained in the CRHB+LN calculations with the NL3 CEDF. From Ref. [31].

discuss in detail only the band crossings in the Pu isotopes. One can see that apart of ^{250}Cm rather good description of experimental data has been obtained in the CRHB+LN calculations.

The CRHB+LN calculations predict sharp upbend $\Omega_x \sim 0.25$ MeV in all three even-even Pu isotopes [42]. The upbending is complete in ^{244}Pu and the CRHB+LN(NL3*) calculations rather well describe it (Fig.11b); the sharp alignment of the proton $i_{13/2}$ orbitals is a source of this backbending and the neutron $j_{15/2}$ alignment proceeds gradually over extended frequency range. On the contrary, sharp alignments of the proton and neutron pairs take place at the same frequency in the CRHB+LN(NL1) calculations (Fig. 11b) and they somewhat overestimate the kinematic moment of inertia above the band crossing. The same situation with the alignments of the proton $i_{13/2}$ and neutron $j_{15/2}$ pairs exists also in the CRHB+LN(NL1) and CRHB+LN(NL3*) calculations for ^{242}Pu. They accurately reproduce the evolution of kinematic moments of inertia with frequency and the frequency of the paired band crossing (Figs. 8 and 11a). However, since upbending is not complete in experiment it is impossible to judge whether the simultaneous sharp alignments of proton and neutron pairs really take place in nature. The kinematic moment of inertia of the ground state rotational band in ^{246}Pu shows a rapid increase at the highest observed frequencies similar to the one seen before upbendings in ^{242,244}Pu. However, the ^{246}Pu data does not reveal an upbend yet. The upbend in ^{242,244}Pu is predicted $0.01 - 0.02$ MeV earlier in the CRHB+LN(NL3*) calculations as compared with experiment. A similar situation is expected in ^{246}Pu. Considering this and the fact that the last observed point in ^{246}Pu is tentative, one can conclude that there is no significant discrepancies with experimental data. Even better agreement with this new data is seen in the case of the CRHB+LN(NL1) calculations.

Similar CRHB+LN analysis of the paired band crossings in ^{248,250}Cf and ^{246,248,250}Cf (see also Figs. 11d,e and f) has been presented in Ref. [58]. In this reference, the CRHB+LN results for the Cf and Cm nuclei were compared with the ones obtained in the cranked shell model with the pairing correlations treated by a particle-number conserving method (further CSM+PNC) [66]. There are three important differences between the CRHB+LN and CSM+PNC approaches. First, the parameters of the Nilsson potential were carefully adjusted in the CSM+PNC approach to the experimental energies of deformed one-quasiparticle states of actinides in Ref. [66]. Second, in the CSM+PNC approach the deformations are chosen to be close to experimental values and they do not change with rotational frequency. These two types of observables are defined fully self-consistently in the CRHB+LN approach without any fit to experimental data, and, in addition, the deformations (mass moments) change with rotational frequency (Fig. 10d). Third, the pairing strength has been fitted to experiment in both approaches [42, 66]. However, the pairing strength is different in even-even and odd-mass nuclei in the CSM+PNC approach [66]; this is a well known deficiency

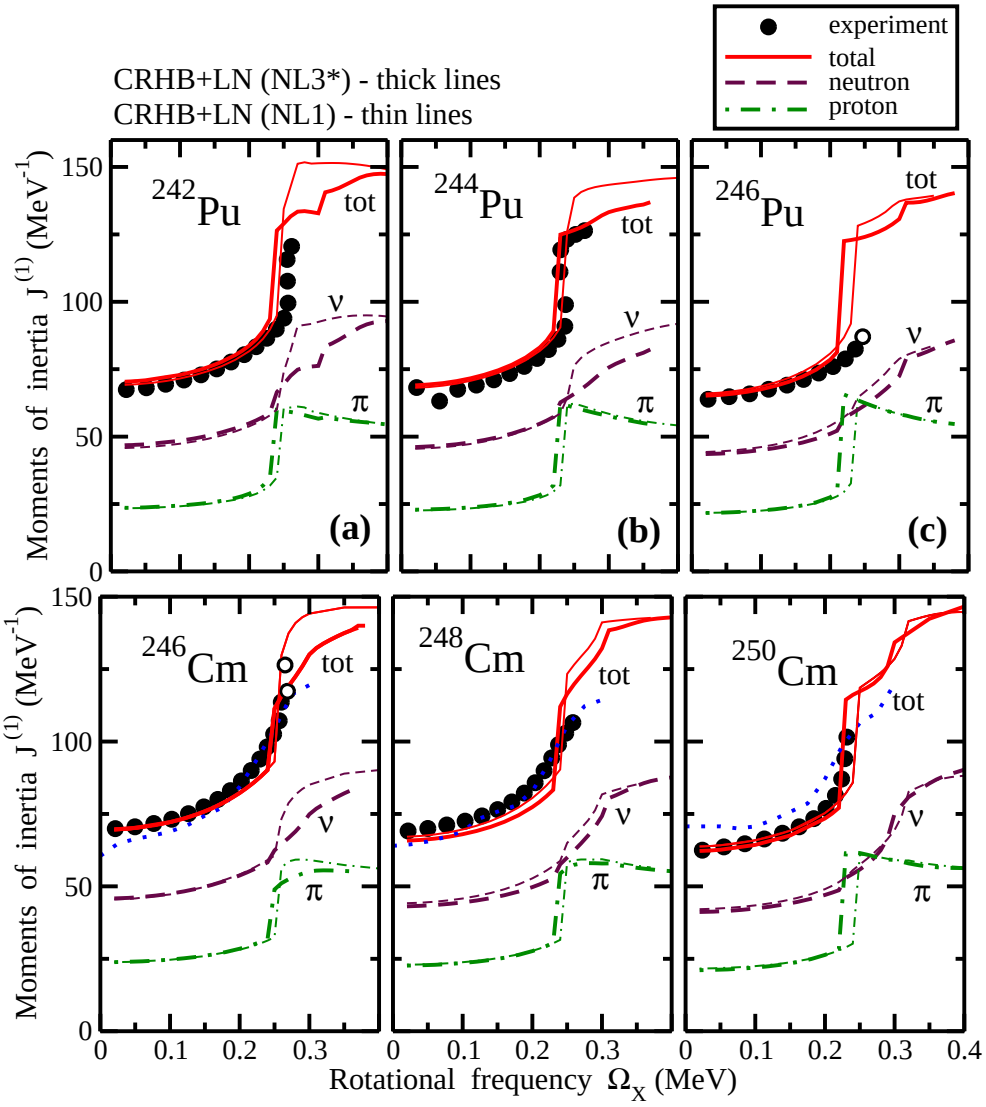

FIG. 11. The experimental and calculated kinematic moments of inertia $J^{(1)}$ of ground state rotational bands in indicated nuclei as a function of rotational frequency Ω_x. Proton and neutron contributions to the kinematic moment of inerta are presented. Open circles are used for tentative experimental points. Total kinematic moments of inertia obtained in the CSM+PNC approach [66] are shown by blue solid lines. Based on Ref. [58].

of the cranked shell model (see, for example, Ref. [67]). In contrast, the same pairing strength is used in even-even and odd-mass nuclei in the CRHB+LN approach; it leads to a consistent and accurate description of odd-even mass staggerings (the $\Delta^{(3)}$ indicators) and the moments of inertia in even-even and odd-mass actinides (see Ref. [42] and Sect. VI).

Thus, CRHB+LN approach provides much more consistent description of rotational properties in paired regime as compared with the CSM+PNC approach; with no adjustment of single-particle energies and deformations to experiment it obtains comparable in accuracy description of experimental rotational properties of actinides [58]. In addition to these studies in actinides, the CRHB+LN approach has succefully been applied to the investigations of the ground state rotational bands in the $A \sim 70$ $N \sim Z$ region [68] and of the evolutions of the moments of inertia with particle numbers at low frequency ($\Omega_x = 0.02$ MeV) in the rare-earth region [41].

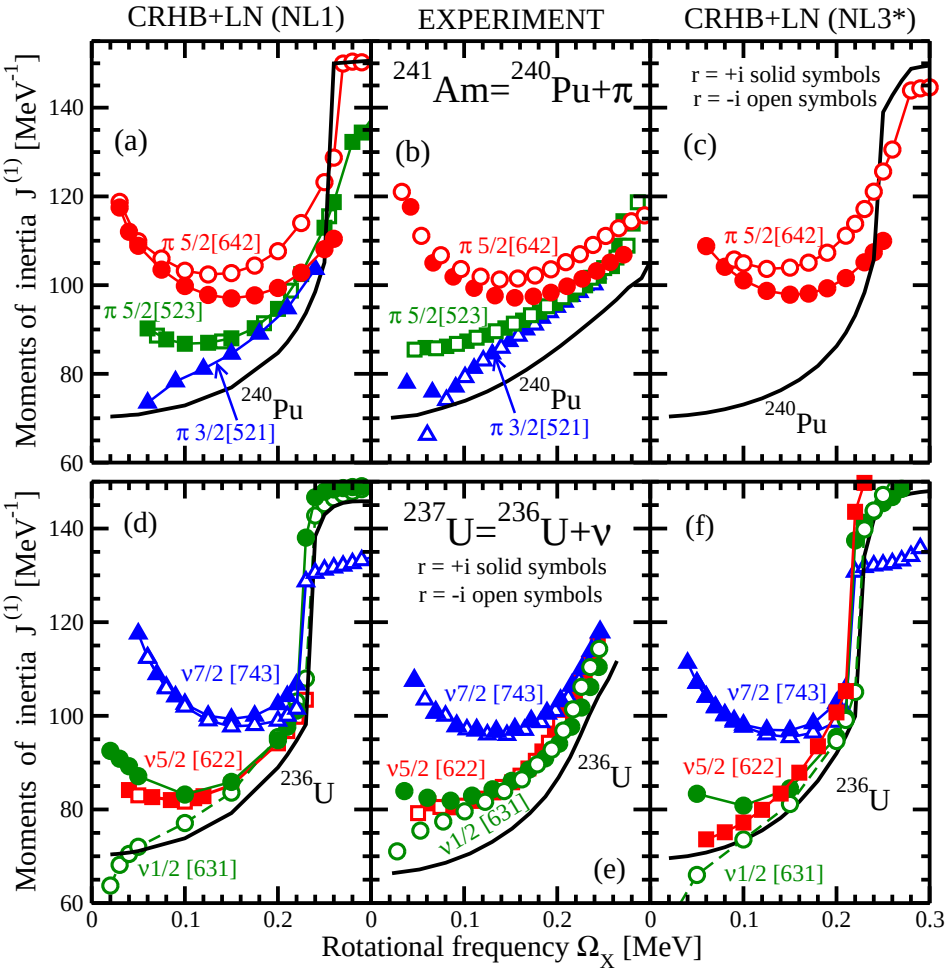

FIG. 12. (top panels) Calculated and experimental kinematic moments of inertia $J^{(1)}$ of the indicated one-quasiproton configurations in the ^{241}Am nucleus and ground state rotational band in reference even-even ^{240}Pu nucleus. Experimental data are shown in the middle panel, while the results of the CRHB+LN calculations with the NL1 and NL3* CEDF's in the left and right panels, respectively. The same symbols/lines are used for the same theoretical and experimental configurations. The symbols are used only for the configurations in odd-mass nucleus; the ground state rotational band in reference even-even nucleus is shown by solid black line. The label with the following structure "Odd nucleus = reference even+even nucleus + proton(π)/neutron(ν)" is used in order to indicate the reference even-even nucleus and the type of the particle (proton or neutron) active in odd-mass nucleus. (bottom panels) The same as in top panels but for one-quasineutron configurations in ^{237}U and ground state band in ^{236}U. The experimental data are from Refs. [69, 70]. Based on Ref. [42].

VI. ROTATIONAL BANDS OF ODD-MASS NUCLEI IN PAIRED REGIME

In the DFT framework, the description of rotational bands in odd-mass nuclei is more technically difficult than the one in even-even nuclei because of the reasons discussed below. The systematic study of such bands has so far been performed only in CDFT [42].

First, the effects of blocking due to odd particle have to be included in a fully self-consistent way. This is done in the CRHB+LN computer code according to Refs. [36, 71, 72]. In addition, it requires the identification of blocked orbital at all frequencies of interest which is non-trivial problem. In the CRHB+LN code [31, 42] the blocked orbital can be specified by different fingerprints such as

- dominant main oscillator quantum number N of the wave function,
- the dominant Ω quantum number (Ω is the projection of the angular momentum on the symmetry axis) of the wave function,
- the particle or hole nature of the blocked orbital,

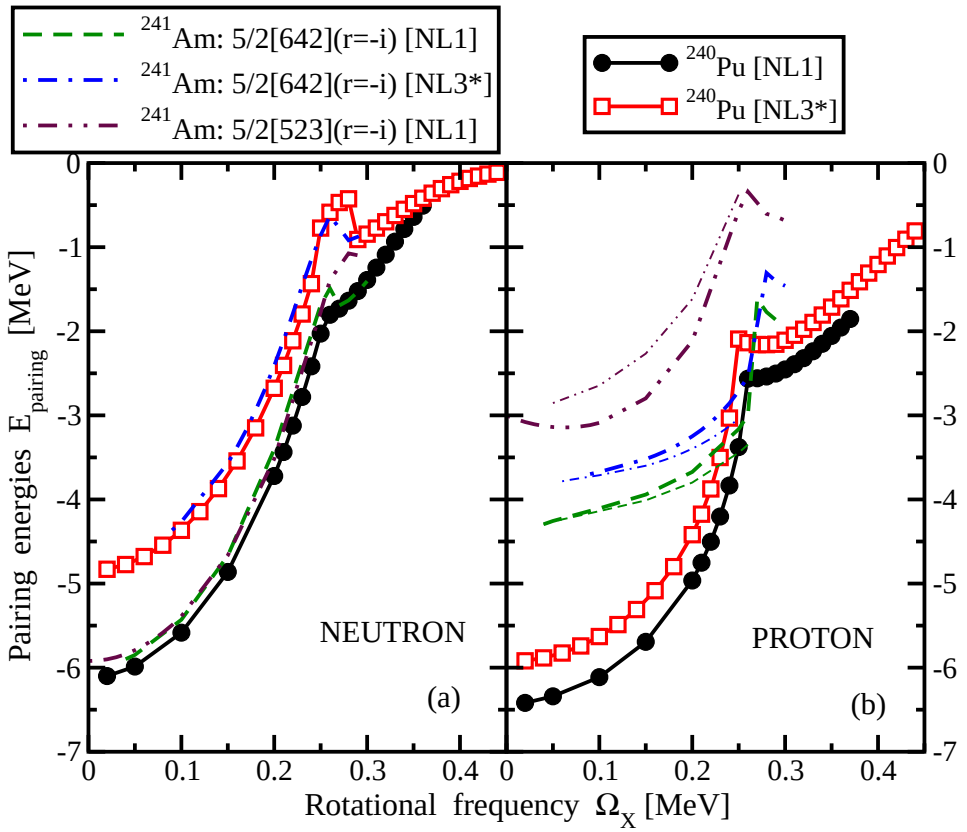

FIG. 13. Calculated proton and neutron pairing energies in ground state rotational band of ^{240}Pu and one-quasiproton rotational bands of ^{241}Am. Thick and thin lines are used for the $(r = -i)$ and $(r = +i)$ branches of one-quasiparticle configurations, respectively. Note that neutron pairing almost does not depend on the signature of blocked proton orbital. As a result, only the $(r = -i)$ branches are shown in panel (a). From Ref. [42].

- the position of the state within specific parity/signature/dominant N/dominant Ω block,

or their combination. For a given configuration, possible combinations of the blocked orbital fingerprints were defined from the analysis of calculated quasiparticle spectra in neighboring even-even nuclei and the occupation probabilities of the single-particle orbitals of interest in these nuclei.

Second, variational calculations with blocked orbital(s) are numerically less stable than the ones for the ground state bands in even-even nuclei because at each iteration of the variational procedure blocked orbital has to be properly identified. The convergence problems are the consequence of the fact that closely lying orbitals within a given parity/signature block interact and exchange a character; the strength of the interaction is important factor here. Another ingredient affecting the convergence is the relative energies of interacting orbitals. Different CEDF's are characterized by different single-particle spectra [73]. As a result, the convergence problems for specific blocked solution can show up in one functional but will not affect the solution in another one. A detailed discussion of the convergence problems in the calculations of rotational bands in odd-mass nuclei and the ways to overcome them is presented in Sect. V of Ref. [42].

Fig. 12 displays a representative example of the RHB+LN calculations for one-quasiparticle bands in ^{237}Np and ^{241}Am which come from systematical studies of Ref. [42]. Additional results for ^{253}No and ^{255}Lr can be found in Refs. [74, 75][4]. In ^{241}Am, the rotational bands based on the Nilsson orbitals $\pi 5/2[642]$ (from the $i_{13/2}$ spherical subshell), $\pi 5/2[523]$ (from the $h_{9/2}$ subshell) and $\pi 3/2[521]$ (from the $f_{7/2}$ subshell) have been observed; their kinematic moments of inertia $J^{(1)}$ are distinctly different at low frequencies. Theoretical calculations (Fig. 12a,c) describe well the absolute values of the kinematic moments of inertia of different configurations, their evolution with rotational frequency and signature splitting. They also indicate that the results of the RHB+LN calculations for a specific configuration only weakly depend on CEDF. Above mentioned features are also clearly seen in ^{237}Np.

[4] To my knowledge, in the DFT framework two-quasiparticle rotational bands have been calculated only in a single case of ^{74}Rb [76] and again in the CRHB+LN approach

Figs. 12a and c also shows that the convergence depends on CEDF. Indeed, it was not possible to get convergent solutions for the $\pi 5/2[523]$ and $\pi 3/2[521]$ configurations of ^{241}Am in the calculations with the NL3* CEDF.

The increase of the kinematic moment of inertia in the bands of ^{241}Am as compared with the one of the ground state band in ^{240}Pu (Fig. 12) is caused by the blocking effect which results in a decreased proton pairing (see Fig. 13). This figure also shows that the blocking of proton orbitals almost does not affect the pairing in neutron subsystem.

The systematic studies of Ref. [42] allowed to conclude that rotational properties of one-quasiparticle configurations substantially depend on the structure of blocked orbital. As a result, the rotational properties reflected through the following fingerprints

- the presence or absence of signature splitting,
- the relative properties of different configurations with respect of each other and/or with respect to the ground state band in reference even-even nucleus,
- the absolute values of the kinematic moments of inertia (especially at low rotational frequencies) and their evolution with rotational frequency

provide useful tools for quasiparticle configuration assignments. Such configuration assignments are important, for example, for on-going experimental investigations of odd-mass light superheavy nuclei at the edge of the region where spectroscopic studies are still feasible (the nuclei with masses $A \sim 255$ and proton number $Z \geq 102$) [42, 77]. Ref. [42] clearly showed that with few exceptions these features of rotational bands are well described in the RHB+LN calculations. The presence or absence of signature separation and its magnitude is the most reliable fingerprint which is reproduced in model calculations with good accuracy. The moments of inertia and their evolution with frequency are generally well described in model calculations. As a consequence, the relative properties of different configurations with respect of each other and/or with respect to the ground state band in reference even-even nucleus provide a reasonably reliable fingerprint of configuration.

However, it is necessary to recognize that the configuration assignment based on rotational properties has to be complemented by other independent methods and has to rely on sufficient experimental data [42]. This is because such method of configuration assignment not always leads to a unique candidate configuration due to theoretical inaccuracies in the description of the moments of inertia.

The ability to calculate odd-mass nuclei fully self-consistently with allowance of nuclear magnetism and breaking of Kramer's degeneracy has also allowed to address the question of consistency of the definition of pairing strength in CDFT. The strengths of pairing defined by means of the kinematic moments of inertia $J^{(1)}$ and three-point $\Delta^{(3)}$ indicators

$$\Delta^{(3)}_{\nu}(N) = \frac{(-1)^N}{2}\left[B(N-1) + B(N+1) - 2B(N)\right], \tag{23}$$

defined from odd-even staggering of binding energies $B(N)$ (similar expression holds also for proton $\Delta^{(3)}_{\pi}$ indicator), strongly correlate [42]. This is known result in non-selfconsistent models based on phenomenological Woods-Saxon or Nilsson potentials. However, this is non-trivial result in the DFT framework since time-odd mean fields (absent in phenomenological potentials) strongly affect the moments of inertia [19] and have an impact on three-point $\Delta^{(3)}$ indicators [16]. The definitions of pairing strength via these two observables are complimentary. This is because (i) it is difficult to disentangle proton and neutron contributions to pairing when considering the moments of inertia and (ii) the $\Delta^{(3)}$ indicators are affected by particle-vibration coupling and depend on correct reproduction of the ground states in odd-mass nuclei [42].

VII. HYPERDEFORMATION AT HIGH SPIN

The search for hyperdeformation (HD) at high spin still remains in the focus of attention of nuclear structure community. Although the attempts to observe discrete HD bands at high spin have not been succesful so far, there is a hope that next generation of detectors such as GRETA and AGATA will allow to observe such bands in the future.

Already, some hints of the presence of hyperdeformation at high spin are available. For example, Hyper-Long-HyperDeformed (HLHD) experiment at the EUROBALL-IV γ-detector array revealed some features expected for HD nuclei [78–80]. Although no discrete HD rotational bands have been identified, rotational patterns in the form of ridge-structures in three-dimensional (3D) rotational mapped spectra are identified with dynamic moments of inertia $J^{(2)}$ ranging from 71 to 111 MeV^{-1} in 12 different nuclei selected by charged particle- and/or γ-gating. The four nuclei, ^{118}Te, ^{124}Cs, ^{125}Cs and ^{124}Xe, found with moment of inertia $J^{(2)} \sim 110$ MeV^{-1} are most likely hyperdeformed

[5] while the remaining nuclei with smaller values of $J^{(2)}$ are expected to be superdeformed. The width in energy of the observed ridges indicates that there are $\approx 6-10$ transitions in the HD cascades, and a fluctuation analysis shows that the number of bands in the ridges exceeds 10. The HD ridges are observed in the frequency range of about 650 to 800 keV, and their dynamic moments of inertia have typical uncertainty of 10% (e.g. 111 ± 11 MeV^{-1} in ^{124}Xe).

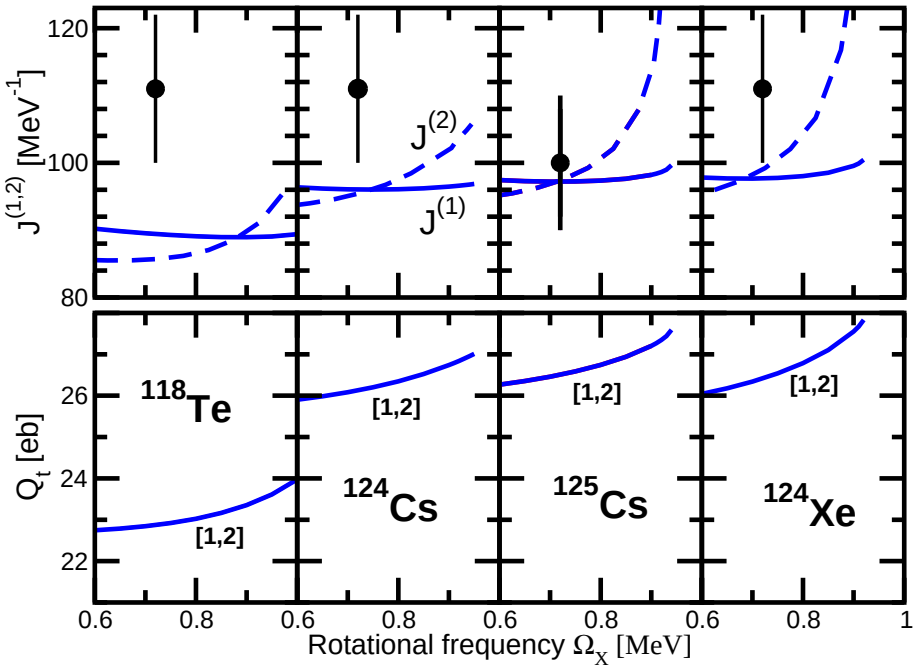

FIG. 14. Calculated kinematic and dynamic moments of inertia (top panels) and transition quadrupole moments (bottom panels) as a function of rotational frequency for the lowest HD solutions in ^{118}Te, ^{124,125}Cs and ^{124}Xe. The structure of calculated configurations is indicated at bottom panels. Experimental data for dynamic moments of inertia of ridge structures are shown in top panels. From Ref. [82].

The experimental data show unusual features never seen before in the studies of the SD bands. For example, the addition of one neutron on going from ^{124}Cs to ^{125}Cs decreases the experimental $J^{(2)}$ value by $\sim 10\%$ (from 111 MeV^{-1} down to 100 MeV^{-1}, see Fig. 14). It is impossible to find an explanation for such a big impact of the single particle on the properties of nuclei: previous studies in the SD minima in different parts of the nuclear chart showed that the addition or removal of particle affects dynamic moments of inertia less drastically [45].

The comparative analysis of the CRMF and CRHB+LN results in ^{124}Xe in Ref. [82] reveals that the pairing is reasonably small in the lowest HD configurations and it becomes even smaller in excited configurations due to blocking effect. The dominant effects in the quenching of pairing correlations are the Coriolis antipairing effect, the quenching due to shell gaps [83], and the blocking effect [36]. Thus, the pairing has been neglected in systematic studies of HD in Ref. [82] in which unpaired CRMF calculations have been performed.

The results of the CRMF calculations with the NL1 CEDF are confronted with experimental data in Fig. 14. The calculated $J^{(2)}$ moments of inertia somewhat underestimate experimental data. The kinematic moments of inertia of the lowest HD solutions are either nearly constant or very gradually increase with rotational frequency. On the contrary, both the dynamic moments of inertia and the transition quadrupole moment Q_t more rapidly increase with rotational frequency over the calculated frequency range. They are in complete contract to the features of the SD bands in unpaired regime, in which the Q_t, $J^{(1)}$ and $J^{(2)}$ values (apart from the unpaired band crossing regions) decrease with increasing rotational frequency (see Refs. [1, 43, 84, 85] and references therein). As discussed in detail in Ref. [82] the microscopic origin of these features lies in a centrifugal stretching of the HD shapes with increasing

[5] In comparison, the HD ridges in ^{152}Dy are characterized by $J^{(2)} \sim 130$ MeV^{-1} [81].

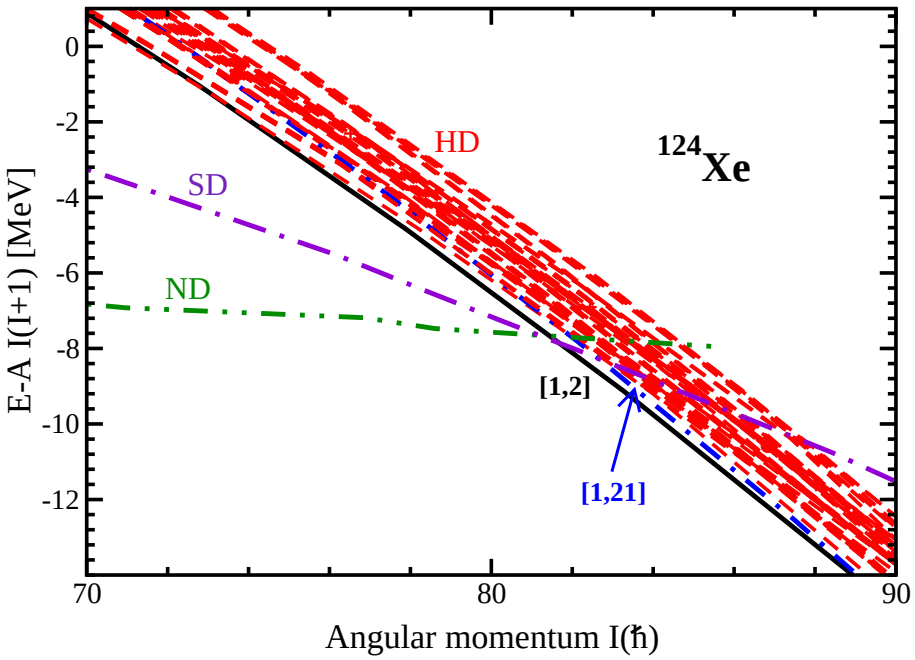

FIG. 15. Energies of the calculated configurations relative to a smooth liquid drop reference $AI(I+1)$, with the inertia parameter $A = 0.01$. The ND and SD yrast lines are shown by dotted and dot-dot-dashed lines, respectively. Solid and dot-dashed lines are used for the [1,2] and [1,21] HD configurations, respectively. Dashed lines represent excited HD configurations. From Ref. [82].

rotational frequency. Systematic analysis of the yrast/near-yrast HD configurations in the part of the nuclear chart studied in Ref. [82] shows that the centrifugal stretching is a general feature of the HD bands.

In order to better understand the general features of HD at high spin I concentrate on the ^{124}Xe nucleus. The results of the CRMF calculations for some HD configurations in ^{124}Xe are displayed in Fig. 15. The calculated configurations are labeled by $[p, n_1 n_2]$, where p, n_1 and n_2 are the number of proton $N = 7$ and neutron $N = 7$ and $N = 8$ hyperintruder orbitals occupied, respectively. For most of the HD configurations, neutron $N = 8$ orbitals are not occupied, so the label n_2 is omitted in the labeling of such configurations. The HD minimum becomes lowest in energy at spin $82\hbar$, and the [1,2] configuration is the yrast HD configuration in the spin range of interest. The excited HD configurations displayed in Fig. 15 are built from this configuration by exciting either one proton or one neutron or simultaneously one proton and one neutron. The total number of excited HD configurations shown is 35. It is interesting to mention that the configuration involving the lowest $N = 8$ neutron orbital (the [1,21] conf. in Fig. 15) is calculated at low excitation energy.

The calculations reveal a high density of the HD configurations which will be even higher if the additional calculations for the excited configurations would be performed starting from the low-lying excited HD configurations, such as the [1,21] configuration. This high density is due to two facts: relatively small $Z = 54$ and $N = 70$ HD shell gaps in the frequency range of interest (see Fig. 10 in Ref. [82] and the softness of the potential energy surfaces in the HD minimum.

With few exceptions mentioned below these two factors are active at hyperdeformation in absolute majority of even-even nuclei in the $Z = 40 - 60$ part of nuclear chart studied in Ref. [82]. Note that different proton and neutron HD gaps will be active in different regions [82]. As a consequence, the density of the HD bands in the spin range where they are yrast or close to yrast is high in the majority of the cases. For such densities, the feeding intensity of an individual HD band will most likely drop below the observational limit of modern experimental facilities so that it will be difficult to observe discrete HD bands. This is because total feeding intensity will be redistributed among many low-lying bands, thus drastically reducing the intensity with which each individual band is populated. On the other hand, the high density of the HD bands may favor the observation of the rotational patterns in the form of ridge-structures in three-dimensional rotational mapped spectra as it has been seen in the HLHD experiment [80]. The study of these patterns as a function of proton and neutron numbers, which seems to be possible with existing facilities, will provide a valuable information about hyperdeformation at high spin.

Only in few nuclei the density of the HD rotational bands is low in the CRMF calculations [82]. These are, for

FIG. 16. (left panels) The self-consistent neutron density $\rho_n(y,z)$ as a function of y- and z- coordinates for the [1,2] configuration in ^{124}Xe at rotational frequency $\Omega_x = 0.75$ MeV. Top and bottom panels show 2- and 3-dimensional plots of the density distribution, respectively. In the top panel, the densities are shown in steps of 0.01 fm^{-3} starting from $\rho_n(y,z) = 0.01$ fm^{-3}. (right panels) The same as left panels, but for yrast megadeformed state in ^{102}Pd at rotational frequency $\Omega_x = 0.95$ MeV. Two top panels show 2-dimensional plots of the proton and neutron densitydistribution. From Ref. [82].

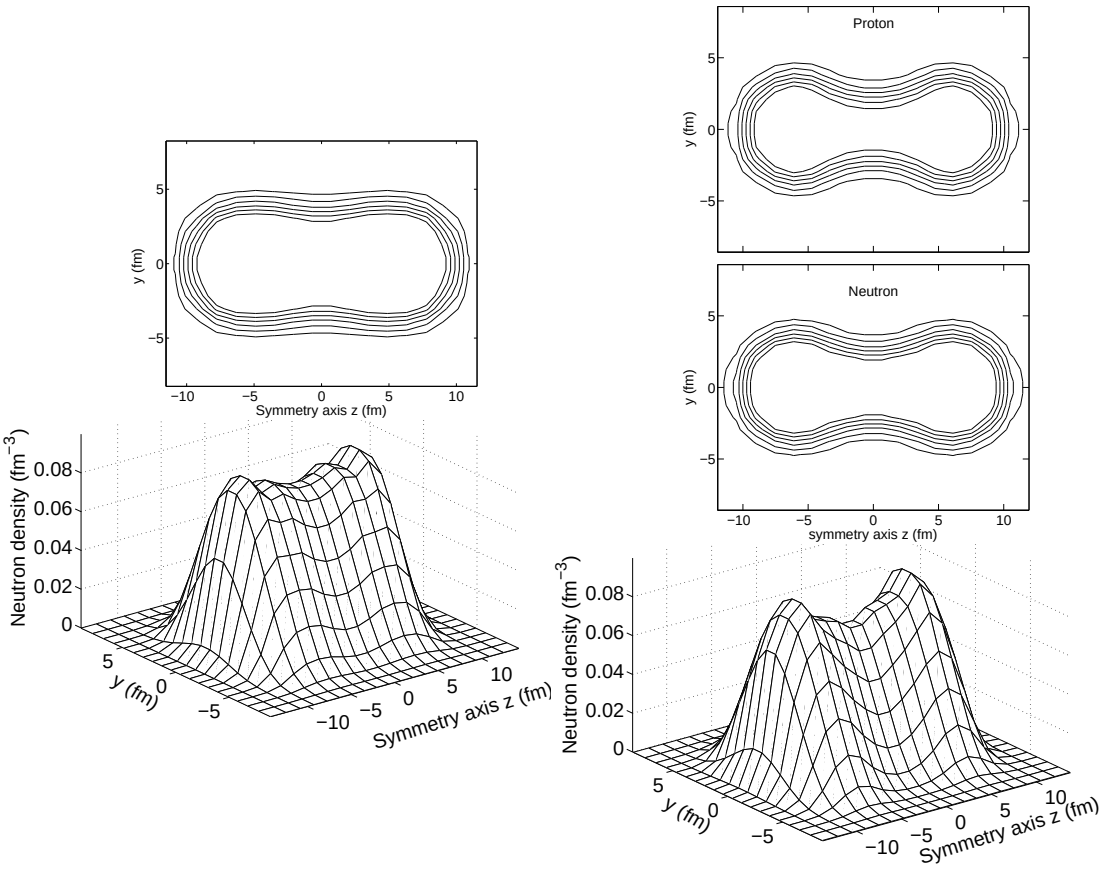

example, ^{96}Cd and ^{107}Cd [86, 87]. The later one is the best candidates for a search of discrete HD bands. An alternative candidate is the doubly magic extremely superdeformed band in ^{111}I [82], the deformation of which is only slightly lower than that of the HD bands, and which may be observed with existing experimental facilities. In all these cases the low density of the HD bands is due to large shell gaps in the single-particle spectra at HD.

Another interesting question is whether necking degree of freedom is important in the HD bands. Fig. 16 shows some indications of the necking and the clusterization of the density into two fragments in the [1,2] configuration of ^{124}Xe, but this effect is not very pronounced in this nucleus. The systematics of the self-consistent proton density distributions in the HD states has been studied in Ref. [82]. In some nuclei (such as ^{124}Te, ^{130}Xe, ^{132}Ba) the necking degree of freedom plays an important role, while others (for example, ^{100}Mo and ^{136}Ce) show no necking. The neck is typically less pronounced in the HD states of the lighter nuclei because of their smaller deformation. In addition, the shell structure also plays a role in a formation of neck. The necking degree of freedom becomes even more important in extremely deformed structures which according to the language of Ref. [88] can be described as megadeformed. Fig. 16 shows an example of density distribution for the megadeformed state in ^{102}Pd, which becomes yrast at $I \sim 85\hbar$ in the CRMF calculations. The neck is more pronounced in the proton subsystem than in the neutron one both in the HD and megadeformed structures due to the Coulomb repulsion of the segments. These results indicate that, in general, the necking degree of freedom is important in the HD states and that it should be treated within the self-consistent approach which, in particular, allows different necking for the proton and neutron subsystems.

The spins I_{cr}^{HD} at which HD bands become yrast (or shortly "crossing spins") represent an important constraint for

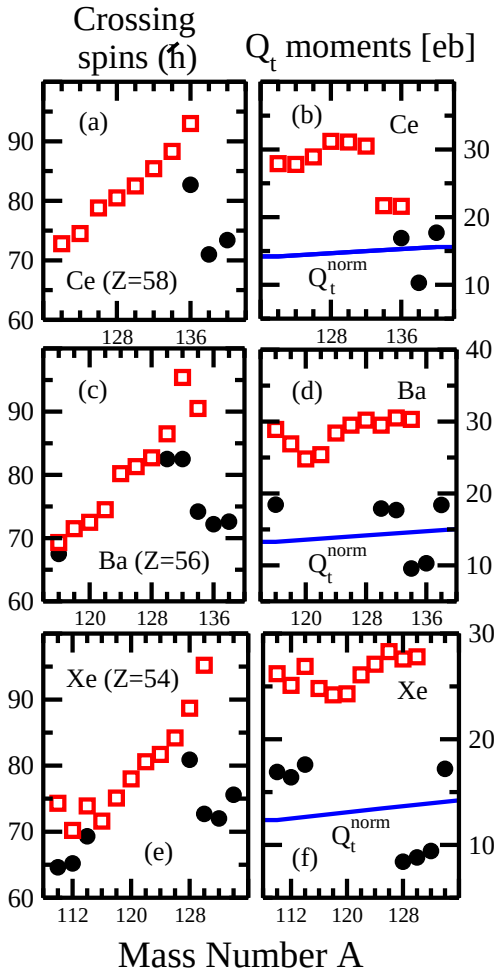

FIG. 17. The crossing spins (left panels) at which the SD (solid circles) and HD (open squares) configurations become yrast and their transition quadrupole moments Q_t (right panels) for the Ce, Ba and Xe isotopes. The values for the SD configurations are shown only in the cases when they become yrast at lower spins than the HD configurations. The normalized transition quadrupole moments Q_t^{norm} corresponding to the deformation of the yrast SD band in ^{152}Dy are shown by blue solid line. Based on Fig. 4 from Ref. [82].

observation of such bands. There are several reasons for that. First, the sensitivity of modern γ-ray detectors defines the highest spins which can be studied in experiment. For example, the GAMMASPHERE allows to study discrete rotational bands only up to $\approx 65\hbar$ in medium mass nuclei [6]. The observation of higher spin states will most likely require a next generation of γ-ray tracking detectors such as GRETA or AGATA. Second, as suggested by the studies of the Jacobi shape transition in Ref. [90], the coexistence of the SD and HD minima at the feeding spins may have an impact on the survival of the HD minima because of the decay from the HD to SD configurations. If this mechanism is active, then only the nuclei in which the HD minimum is lower in energy than the SD one at the feeding spin and/or the nuclei characterized by the large barrier between the HD and SD minima will be the reasonable candidates for a search of the HD bands.

Figs. 17 shows that the HD configurations become yrast at lower spin than the SD ones only in a specific mass range which depends on the isotope chain [82]. It also illustrates that the crossing spins I_{cr}^{HD}, at which the HD configurations become yrast, are lower for proton-rich nuclei. This is a feature seen in the most of studied isotope chains; by going from the β-stability valley towards the proton-drip line one can lower I_{cr}^{HD} by approximately $10\hbar$. In addition, the calculated transition quadrupole moments of these configurations at spin values close to the crossing

[6] The DFT calculations suggest that the triaxial SD band 1 in ^{158}Er is observed up to spin in excess of $70\hbar$ [89]. However, this result requires further experimental confirmation.

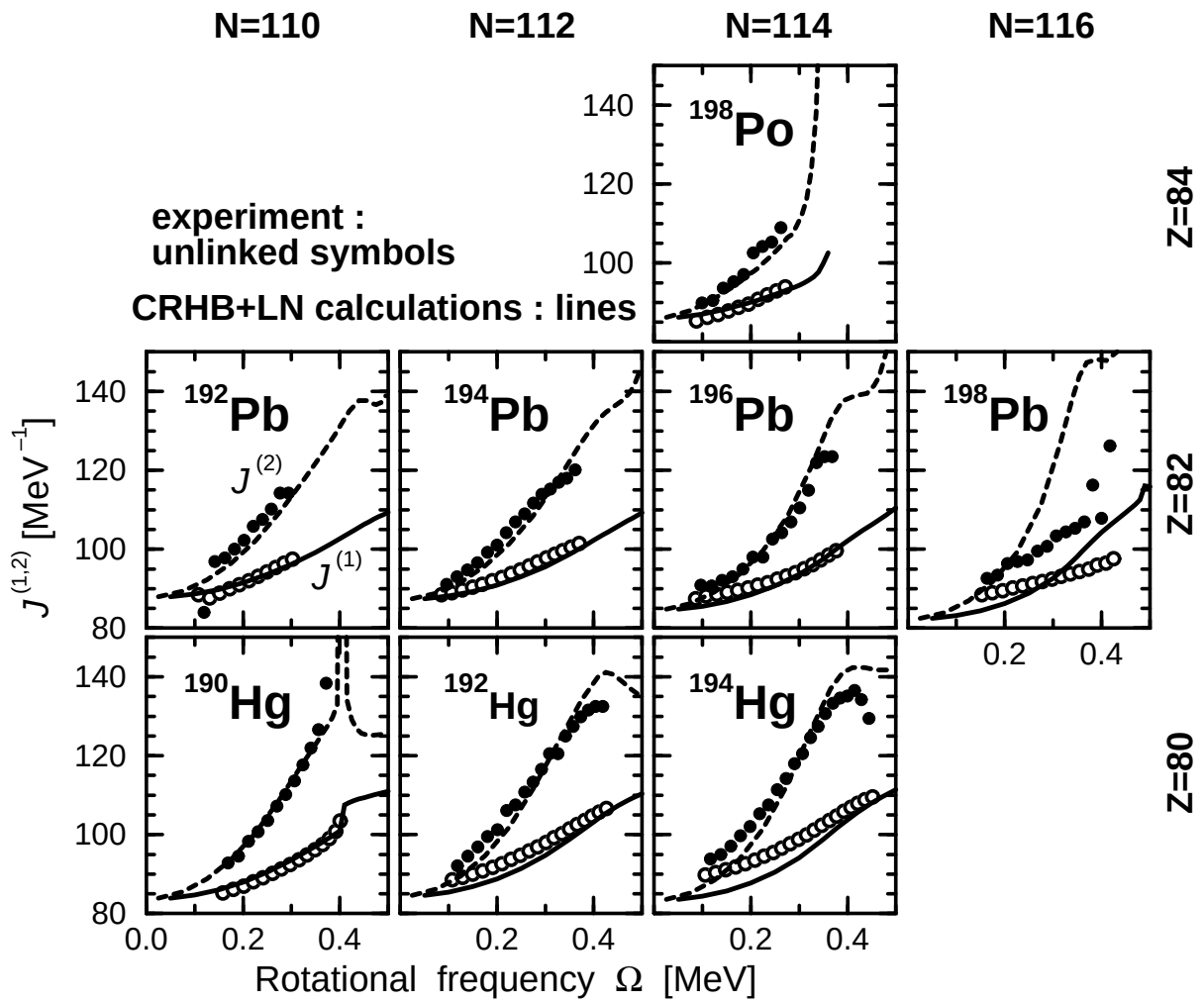

FIG. 18. Kinematic ($\mathcal{J}^{(1)}$) and dynamic ($\mathcal{J}^{(2)}$) moments of inertia of the yrast superdeformed bands in the even-even nuclei of the $A \sim 190$ mass region. Experimental $\mathcal{J}^{(1)}$ and $\mathcal{J}^{(2)}$ values are shown by open and solid circles. Solid and dashed lines are used for the $\mathcal{J}^{(1)}$ and $\mathcal{J}^{(2)}$ values obtained in the CRHB+LN calculations. From Ref. [11].

spins are shown. The calculated HD configurations are near-prolate. Additional results for the Zr, Mo, Ru, Pd, Cd, Sn, Te isotope chains are presented in Ref. [82].

In addition, the single-particle properties and their role in future configuration assignments at HD have been investigated in Ref. [82]. It was concluded that the individual properties of the single-particle orbitals are not lost at HD. In the future, they will allow the assignment of the configurations to the HD bands using the relative properties of different bands. Such methods of configuration assignment were originally developed for superdeformation. In contrast to the case of SD, the analysis of Ref. [82] has showed that only simultaneous application (by comparing experimental and theoretical $(i_{eff}, \Delta Q_t)$ values) of the methods based on effective alignments i_{eff} [91] and relative transition quadrupole moments ΔQ_t [92] will lead to a reliable configuration assignment for the HD bands. Moreover, additional information on the structure of the HD bands will be obtained from the band crossing features; the cases of strong interaction of the bands in unpaired regime at HD will be more common as compared with the situation at SD.

VIII. OTHER PHENOMENA

It is impossible to cover in detail other results obtained for rotational bands within the cranked versions of the CDFT because of space limitations. However, I feel that at least it is necessary to give some short overview of systematic calculations in different mass regions and provide some references on the physical phenomena which have

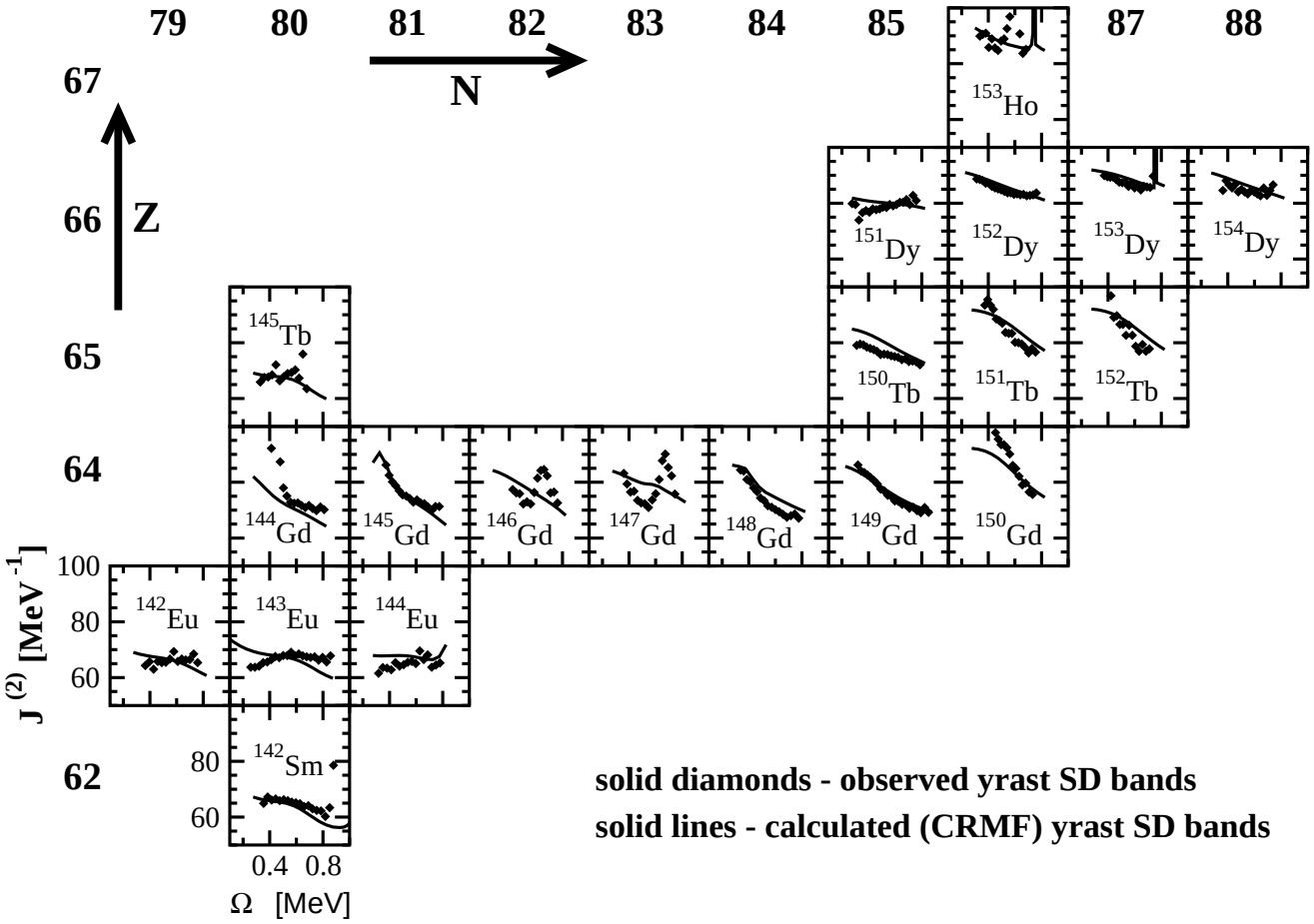

FIG. 19. Dynamic moments of inertia of observed yrast SD bands (solid diamonds) in the $A \sim 140 - 150$ mass region of superdeformation compared with the calculations in cranked RMF theory (solid lines). From Ref. [1].

not been discussed in detail in this review. Note, that transition quadrupole moments are typically described within the error bars of experimental measurements [10, 11, 43, 68, 93]. Thus, we do not consider them below.

A. Superdeformation in paired and unpaired regimes

Results of systematic CRHB+LN calculations with the NL1 CEDF [10, 11] for yrast superdeformed bands in even-even nuclei in the $A \sim 190$ region are shown in Fig. 18. Without any new adjustable parameter a very successful description of rotational features of experimental bands in this region is obtained in the calculations; only in ^{198}Pb the calculations fail to reproduce the kinematic and the dynamic moments of inertia above $\Omega_x \sim 0.25$ MeV (Fig. 18). The increase of the moments of inertia in this mass region can be understood as emerging predominantly from a combination of three effects: the gradual alignment of a pair of $j_{15/2}$ neutrons, the alignment of a pair of $i_{13/2}$ protons at a somewhat higher frequency, and decreasing pairing correlations with increasing rotational frequency. Above $\Omega_x \geq 0.4$ MeV, the $\mathcal{J}^{(2)}$ values determined by the alignment in the neutron subsystem decrease but this process is compensated by the increase of $\mathcal{J}^{(2)}$ due to the continuing alignment of the $i_{13/2}$ proton pair. Thus the shape of the peak (or the plateau) in the total value of $\mathcal{J}^{(2)}$ at these frequencies is determined by a delicate balance between alignments in the proton and neutron subsystems which depends on the deformation, the rotational frequency and the position of the Fermi energy. For example, the alignment of a pair of $j_{15/2}$ neutrons at $\Omega_x \sim 0.4$ MeV is visible experimentally in the isotope ^{192}Hg and even more clearly in ^{194}Hg.

In addition to actinides, the CRHB+LN approach has been used for the yrast SD band in ^{60}Zn in Ref. [47].

A systematic investigation of properties of superdeformed bands in unpaired regime has been performed in the CRMF framework in the $A \sim 60$ [85] and 150 [43, 45] mass regions of superdeformation. It was shown that CRMF theory reproduces in general well the experimentally observed features. For example, a summary of these studies

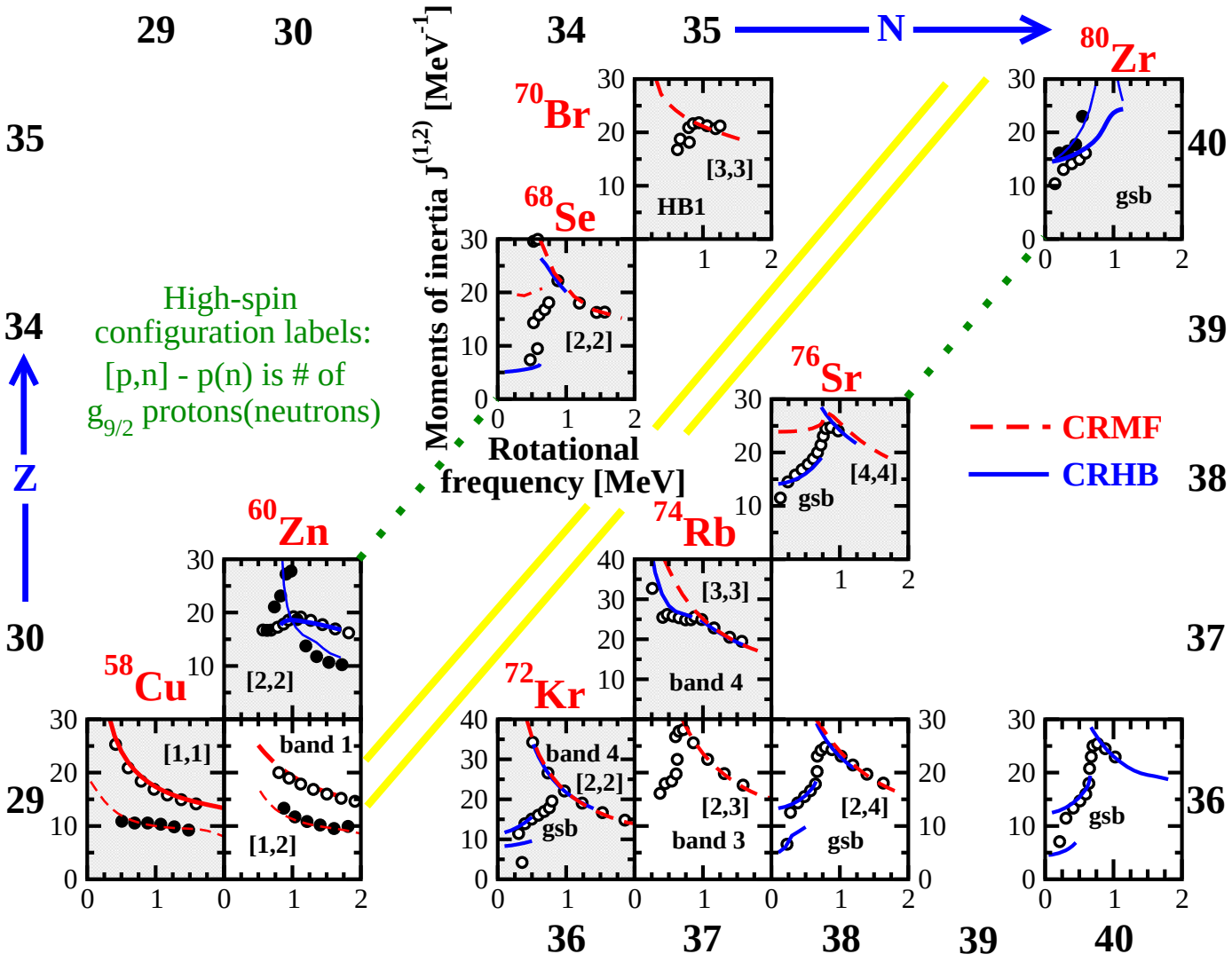

FIG. 20. The kinematic moments of inertia $J^{(1)}$ of rotational structures in the $N \approx Z$ nuclei compared with the results of the CRMF and CRHB+LN calculations. The shaded background is used for $N = Z$ nuclei. The vertical scale of the panels for ^{72}Kr and ^{74}Rb is different from the one of the other panels. Note that in few cases the results for dynamic moments of inertia $J^{(2)}$ are shown. In these cases, thick and thin lines are used for calculated kinematic and dynamic moments of inertia, respectively. Experimental kinematic and dynamic moments of inertia are shown by open and solid circles, respectively. The results of the CRHB+LN calculations at low spin are shown both for prolate and oblate minima in few cases; in a given nucleus calculated $J^{(1)}$ in oblate minimum is lower than the one in prolate minimum.

for the dynamic moments of inertia $\mathcal{J}^{(2)}$ in the $A \sim 150$ region is shown in Fig. 19 and the left corner of Fig. 20 shows the results for the $A \sim 60$ region. I will discuss here the results for $A \sim 150$ mass region. At high rotational frequencies, where pairing is of minor importance, the dynamic moments of inertia are rather well reproduced in the CRMF calculations. Exceptions are the yrast superdeformed bands in ^{146,147}Gd and in ^{153}Ho undergoing unpaired band crossings. For example, in ^{146,147} Gd the peak in $\mathcal{J}^{(2)}$ at $\Omega_x \approx 0.6$ MeV is not reproduced. According to the standard interpretation [45, 91], it originates from the crossing of two specific orbitals with the Nilsson quantum numbers $\nu[651]1/2$ and $\nu[642]5/2$ and signature $r = +i$. The relative position of this pair is not reproduced properly in several RMF parameterizations [43, 45]. Even at low spins, the results of the CRMF calculations are close to experiment in most of the cases. The experiment of Ref. [94] has linked the yrast superdeformed band in ^{152}Dy to the low-spin level scheme which allowed to extract experimental kinematic moment of inertia. Its calculated value is by 7-5% higher than in experiment at low spins and the difference decreases with increasing spin (Ref. [1]. This suggests some persistence of pairing correlations especially at low spins. Note that the systematics of Fig. 19 has recently been extended by the CRMF studies of excited SD bands in ^{154}Dy [95].

B. Neutron-proton pairing

The physics of isoscalar and isovector neutron-proton pairing has been and still is an active topic of nuclear structure studies [93, 96]. At present, the existence of isovector np-pairing is well established. The isovector $np-$pairing is absolutely necessary in order to restore the isospin symmetry of the total wave function. Its strength is well defined by the isospin symmetry. On the contrary, the observed consequences of the $t = 0$ $np-$pairing still remain illusive. The systematic analysis of the rotational response of $N \approx Z$ nuclei performed in the CRHB+LN and CRMF frameworks (see Refs. [68, 93] and references quoted therein) agrees with the picture which does not involve isoscalar $np-$pairing. According to it (isovector mean-field theory [97]), at low spin, an isoscalar $np-$pair field is absent while a strong isovector pair field exists, which includes a large np component, whose strength is determined by isospin conservation. Like in nuclei away from the $N = Z$ line, this isovector pair field is destroyed by rotation. In this high-spin regime, calculations without pairing describe accurately the data (see Fig. 20 and Refs. [68, 93]), provided that the shape changes and band termination are taken into account.

C. Band termination

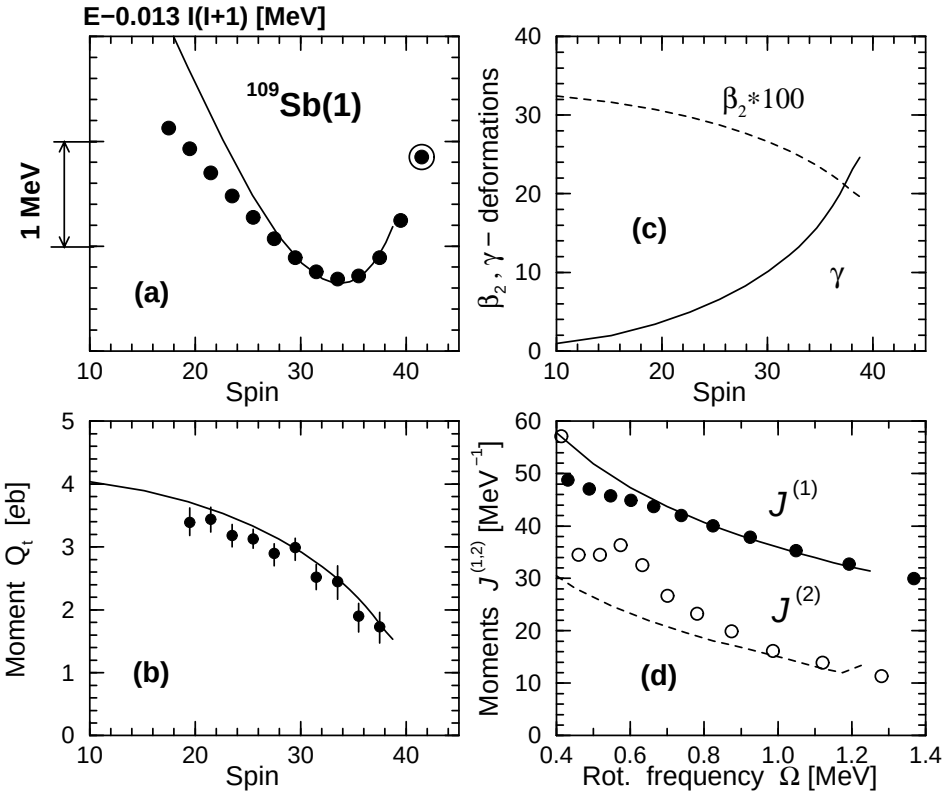

FIG. 21. Smooth terminating band 1 in ^{109}Sb. Circles indicate experimental data, while the results of CRMF calculations are shown by lines. Panel (a) shows the excitation energies relative to a rigid rotor reference $E_{RLD}(I) = 0.013I(I + 1)$ MeV. The terminating state is indicated by a large open circle. The results of the calculations are normalized to experiment at the position of the minima in the $(E - E_{RLD})$ curve. Panel (b) compares measured and calculated transition quadrupole moments Q_t. Calculated β_2 and γ deformations are shown in panel (c). Panel (d) shows the calculated and experimental kinematic and dynamic moments of inertia. From Ref. [1].

Another interesting phenomenon is band termination, and, especially smooth band termination. Smooth terminating band shows a continuous and smooth transition within a specific configuration from a collective rotation to a non-collective terminating (single-particle) state [4]. The band terminates in the terminating state which shows full alignment of all angular momentum vectors of the valence particles and holes along the axis of rotation. In the CDFT framework, the band termination phenomenon has been studied only in a few cases. One of them is ground

state band in ^{20}Ne terminating at $I = 8^+$; this is a classical case of band termination. The termination of this band and the impact of time-odd mean fields on its rotational properties and terminating state have been studied in Ref. [22]. In addition, the impact of these fields on the binding energies of terminating states in the $A \sim 44$ region has been studied in Ref. [22]. Fig. 21 presents the only case of the study of smooth band termination in the CRMF framework; this is smooth terminating band 1 in ^{109}Sb. One can see that experimental observables shown in Fig. 21 are well described in the CRMF calculations at $\Omega_x \geq 0.8$ MeV (above $I \geq 25\ \hbar$) where pairing is expected to play a minor role. The discrepancies between experiment and theory seen at lower spins are probably due to neglect of the pairing correlations in the CRMF calculations. One should note that without special techniques (as developed in cranked Nilsson-Strutinsky approach [4]) it is impossible to trace this configuration in the CRMF calculations up to its terminating state.

It is necessary to recognize that not all rotational bands will terminate in non-collective terminating state at the maximum spin I_{max} [4]. So far the examples of non-termination of rotational bands at the maximum spin have been experimentally observed and studied in the CRMF framework only in ^{74}Kr and ^{75}Rb [98, 99].

D. Other results

Other phenomena in rotating nuclei or the features of rotational bands have been studied in the CRMF/CRHB frameworks during last decade. They will only be briefly mentioned here.

The additivity principle for quadrupole moments and relative alignments has been studied on the example of highly-deformed and superdeformed bands in the $A \sim 130$ mass region in Ref. [100]. This principle of the extreme shell model stipulates that an average value of a one-body operator be equal to the sum of the core contribution and effective contributions of valence (particle or hole) nucleons. It is only valid in an unpaired regime typical of high angular momenta since the pairing smears out the individuality of each single-particle orbital. The additivity principle for angular momentum alignments does not work as precisely as it does for quadrupole moments.

Triaxial superdeformed (TSD) rotational bands at ultra-high spin in the Er region have been studied on the example of ^{158}Er in Ref. [89]. Good description of the deformation and rotational properties of the TSD bands observed in this nucleus has been achieved in the CRMF calculations. Based on the results of covariant and non-relativistic DFT calculations it was suggested that the TSD band 1 in this nucleus is observed up to spin in excess of $70\hbar$ [89] which is the highest spin reported so far. The enhanced deformation and SD bands in the Hf isotopes have been investigated in Ref. [101]. Contrary to previous claims of triaxiality of the SD bands in ^{175}Hf, the bands in this nucleus are interpreted in the CRMF framework as near-prolate. However, it was concluded that some SD bands in less neutron-rich Hf isotopes may be triaxial.

Theoretical uncertainties in the description of the physical observables of rotational bands (deformations, moments of inertia and their evolution with spins, band crossing frequencies and alignment gains at band crossings etc) and their dependence on CEDF have been analyzed in Ref. [102].

IX. CONCLUSIONS

The systematic studies of different types of rotational bands (normal-deformed, smooth terminating, superdeformed and hyperdeformed) have been performed in one-dimensional cranking approximation of the CDFT in different regions of nuclear chart from ground states to the extremes of deformation and spin. Contrary to the studies of rotating nuclei in non-relativistic DFT models, the CDFT studies have been performed systematically covering large amount of experimental data in the region of study. The CRMF and CRHB+LN calculations succesfully describe the experimental situation and in many cases they outperform non-relativistic models. The rotating nuclei offer a unique laboratory for testing of the channels of the CDFT which are not accessible by other physical observables. This is because their properties sensitively depend on nuclear magnetism (time-odd mean fields) and underlying single-particle structure. The part of the success of the CDFT in the description of rotating nuclei is definitely attributable to the fact that time-odd mean fields are uniquely defined via Lorentz covariance.

Acknowledgements

This material is based upon work supported by the U.S. Department of Energy, Office of Science, Office of Nuclear

Physics under Award No. de-sc0013037.

---

[1] D. Vretenar, A. V. Afanasjev, G. A. Lalazissis, and P. Ring, Phys. Rep. **409**, 101 (2005).
[2] M. Bender, P.-H. Heenen, and P.-G. Reinhard, Rev. Mod. Phys. **75**, 121 (2003).
[3] C. Baktash, B. Haas, and W. Nazarewicz, Annu. Rev. Nucl. Part. Sci. **45**, 485 (1995).
[4] A. V. Afanasjev, D. B. Fossan, G. J. Lane, and I. Ragnarsson, Phys. Rep. **322**, 1 (1999).
[5] S. Frauendorf, Rev. Mod. Phys. **73**, 463 (2001).
[6] J. Meng, J. Peng, S.-Q. Zhang, and P.-W. Zhao, Front. Phys. **8**, 55 (2013).
[7] J. König and diploma thesis Technical University of Munich (unpublished), (1996).
[8] W. Koepf and P. Ring, Nucl. Phys. A **493**, 61 (1989).
[9] H. Madokoro and M. Matsuzaki, Phys. Rev. C **56**, R2934 (1997).
[10] A. V. Afanasjev, J. König, and P. Ring, Phys. Rev. C **60**, 051303 (1999).
[11] A. V. Afanasjev, P. Ring, and J. König, Nucl. Phys. **A676**, 196 (2000).
[12] D. R. Inglis, Phys. Rev. **103**, 1786 (1956).
[13] B. D. Serot and J. D. Walecka, Adv. Nucl. Phys. **16**, 1 (1986).
[14] P.-G. Reinhard, M. Rufa, J. Maruhn, W. Greiner, and J. Friedrich, Z. Phys. A **323**, 13 (1986).
[15] A. R. Edmonds, *Angular Momentum in Quantum Mechanics* (Princeton University Press, 1957).
[16] A. V. Afanasjev and H. Abusara, Phys. Rev. C **81**, 014309 (2010).
[17] A. V. Afanasjev and P. Ring, Phys. Rev. C **62**, 031302(R) (2000).
[18] J. König and P. Ring, Phys. Rev. Lett. **71**, 3079 (1993).
[19] A. V. Afanasjev and H. Abusara, Phys. Rev. C **82**, 034329 (2010).
[20] J. Dobaczewski and J. Dudek, Phys. Rev. C **52**, 1827 (1995).
[21] M. Yamagami and K. Matsuyanagi, Nucl. Phys. A **672**, 123 (2000).
[22] A. V. Afanasjev, Phys. Rev. C **78**, 054303 (2008).
[23] U. Hofmann and P. Ring, Phys. Lett. B **214**, 307 (1988).
[24] Y. M. Engel, D. M. Brink, K. Geoke, S. J. Krieger, and D. Vauterin, Nucl. Phys. A **249**, 215 (1975).
[25] V. O. Nesterenko, W. Kleinig, J. Kvasil, P. Vesely, and P.-G. Reinhard, Int. J. Mod. Phys. E **17**, 89 (2008).
[26] N. Hinohara, T. Nakatsukasa, M. Matsuo, , and K. Matsuyanagi, Prog. Theor. Phys. **115**, 567 (2006).
[27] A. S. Umar and V. E. Oberacker, Phys. Rev. C **73**, 054607 (2006).
[28] M. Bender, J. Dobaczewski, J. Engel, and W. Nazarewicz, Phys. Rev. C **65**, 054322 (2002).
[29] W. Satula, in *Nuclear Structure 98*, edited by C. Baktash, AIP Conf. Proc. No. 481 (AIP, New York, 1999) , 114 (1999).
[30] T. Duguet, P. Bonche, P.-H. Heenen, and J. Meyer, Phys. Rev. C **65**, 014310 (2001).
[31] A. V. Afanasjev, T. L. Khoo, S. Frauendorf, G. A. Lalazissis, and I. Ahmad, Phys. Rev. C **67**, 024309 (2003).
[32] K. Rutz, M. Bender, P.-G. Reinhard, and J. A. Maruhn, Phys. Lett. B **468**, 1 (1999).
[33] J. F. Berger, M. Girod, and D. Gogny, Nucl. Phys. **A428**, 23c (1984).
[34] L. J. Wang, B. Y. Sun, J. M. Dong, and W. H. Long, Phys. Rev. C **87**, 054331 (2013).
[35] S. E. Agbemava, A. V. Afanasjev, D. Ray, and P. Ring, Phys. Rev. C **89**, 054320 (2014).
[36] P. Ring and P. Schuck, *The nuclear many-body problem* (Springer-Verlag, New York, 1980).
[37] H. J. Lipkin, Ann. Phys. **9**, 272 (1960).
[38] Y. Nogami, Phys. Rev. **134**, 313 (1964).
[39] Y. Nogami and I. Zucker, Nucl. Phys. **60**, 203 (1964).
[40] H. C. Pradhan, Y. Nogami, and J. Law, Nucl. Phys. A **201**, 357 (1973).
[41] A. V. Afanasjev, J. König, P. Ring, L. M. Robledo, and J. L. Egido, Phys. Rev. C **62**, 054306 (2000).
[42] A. V. Afanasjev and O. Abdurazakov, Phys. Rev. C **88**, 014320 (2013).
[43] A. V. Afanasjev, J. König, and P. Ring, Nucl. Phys. A **608**, 107 (1996).
[44] W. Koepf and P. Ring, Nucl. Phys. A **511**, 279 (1990).
[45] A. V. Afanasjev, G. Lalazissis, and P. Ring, Nucl. Phys. A **634** (1998).
[46] H. Molique, J. Dobaczewski, and J. Dudek, Phys. Rev. C **61**, 044304 (2000).
[47] A. V. Afanasjev, P. Ring, and I. Ragnarsson, Proc. Int. Workshop PINGST2000 "Selected topics on $N = Z$ nuclei", 2000, Lund, Sweden, Eds. D. Rudolph and M. Hellström , 183 (2000).
[48] K.-K. Kan and J. J. Griffin, Phys. Rev. C **15**, 1126 (1977).
[49] M. Durand, P. Schuck, and J. Kunz, Nucl. Phys. A **439**, 263 (1985).
[50] I. Mikhailov, P. Quentin, and D. Samsoen, Nucl. Phys. A **627**, 259 (1997).
[51] H. Laftchiev, D. Samsœn, P. Quentin, and I. N. Mikhailov, Phys. Rev. C **67**, 014307 (2003).
[52] M. Radomski, Phys. Rev. C **14**, 1704 (1976).
[53] P. Gulshani and D. J. Rowe, Can. J. Phys. **56**, 468 (1978).
[54] P. Gulshani and D. J. Rowe, Can. J. Phys. **56**, 480 (1978).
[55] J. Kunz and U. Mosel, Nucl. Phys. A **323**, 271 (1979).
[56] J. Fleckner, J. Kunz, U. Mosel, and E. Wuest, Nucl. Phys. A **339**, 227 (1980).
[57] A. Bohr and B. R. Mottelson, *NUCLEAR STRUCTURE Volume II: Nuclear Deformation* (W. A. Benjamin, Inc., 1975).

[58] A. V. Afanasjev, Phys. Scr. **89**, 054001 (2014).
[59] J. Egido and L. Robledo, Nucl. Phys. A **570**, 69 (1994).
[60] M. Anguiano, J. Egido, and L. Robledo, Nucl. Phys. A **683**, 227 (2001).
[61] M. Anguiano, J. Egido, and L. Robledo, Nucl. Phys. A **696**, 467 (2001).
[62] T. Duguet, P. Bonche, and P.-H. Heenen, Nucl. Phys. A **679**, 427 (2001).
[63] M. Bender, P. Bonche, T. Duguet, and P.-H. Heenen, Nucl. Phys. A **723**, 354 (2003).
[64] G. A. Lalazissis, S. Karatzikos, R. Fossion, D. P. Arteaga, A. V. Afanasjev, and P. Ring, Phys. Lett. **B671**, 36 (2009).
[65] S. Hota, PhD thesis, University of Massachussets, Lowell (2012).
[66] Z.-H. Zhang, X.-T. He, J.-Y. Zeng, E.-G. Zhao, and S.-G. Zhou, Phys. Rev. C **85**, 014324 (2012).
[67] S. K. Tandel, P. Chowdhury, S. Lakshmi, U. S. Tandel, I. Ahmad, M. P. Carpenter, S. Gros, R. V. F. Janssens, T. L. Khoo, F. G. Kondev, J. P. Greene, D. J. Hartley, T. Lauritsen, C. J. Lister, D. Peterson, A. Robinson, D. Seweryniak, and S. Zhu, Phys. Rev. C **82**.
[68] A. V. Afanasjev and S. Frauendorf, Phys. Rev. C **71**, 064318 (2005).
[69] X. Wang, R. V. F. Janssens, M. P. Carpenter, S. Zhu, I. Wiedenhöver, U. Garg, S. Frauendorf, T. Nakatsukasa, I. Ahmad, A. Bernstein, E. Diffenderfer, S. J. Freeman, J. P. Greene, T. L. Khoo, F. G. Kondev, A. Larabee, T. Lauritsen, C. J. Lister, B. Meredith, D. Seweryniak, C. Teal, and P. Wilson, Phys. Rev. Lett. **102**, 122501 (2009).
[70] K. Abu Saleem, R. V. F. Janssens, M. P. Carpenter, F. G. Kondev, I. Wiedenhöver, I. Ahmad, J. Caggiano, P. Chowdhury, J. A. Cizewski, D. Cline, M. Devlin, N. Fotiades, J. P. Greene, G. Hackman, A. Heinz, T. L. Khoo, T. Lauritsen, C. J. Lister, A. O. Macchiavelli, E. H. Seabury, D. Seweryniak, A. Sonzogni, and C. Y. Wu, Phys. Rev. C **70**, 024310 (2004).
[71] P. Ring, R. Beck, and H. J. Mang, Z. Phys. **231**, 10 (1970).
[72] J. L. Egido, H. J. Mang, and P. Ring, Nucl. Phys. A **334**, 1 (1980).
[73] A. V. Afanasjev and S. Shawaqfeh, Phys. Lett. B **706**, 177 (2011).
[74] R.-D. Herzberg, S. Moon, S. Eeckhaudt, P. T. Greenlees, P. A. Butler, T. Page, A. V. Afanasjev, N. Amzal, J. E. Bastin, F. Becker, M. Bender, B. Bruyneel, J. F. C. Cocks, I. G. Darby, O. Dorvaux, K. Eskola, J. Gerl, T. Grahn, C. Gray-Jones, N. J. Hammond, K. Hauschild, P.-H. Heenen, K. Helariutta, A. Herzberg, F. Hessberger, M. Houry, A. Hürstel, R. D. Humphreys, G. D. Jones, P. M. Jones, R. Julin, S. Juutinen, H. Kankanpää, H. Kettunen, T. L. Khoo, W. Korten, P. Kuusiniemi, Y. LeCoz, M. Leino, A.-P. Leppanen, C. J. Lister, R. Lucas, M. Muikku, P. Nieminen, M. Nyman, R. D. Page, T. Page, J. Pakarinen, A. Pritchard, P. Rahkila, P. Reiter, M. Sandzelius, J. Saren, C. Schlegel, C. Scholey, C. Theisen, W. H. Trzaska, J. Uusitalo, A. Wiens, and H. J. Wollersheim, Eur. Phys. J. **A42**, 333 (2009).
[75] H. B. Jeppesen, R. M. Clark, K. E. Gregorich, A. V. Afanasjev, M. N. Ali, J. M. Allmond, C. W. Beausang, M. Cromaz, M. A. Deleplanque, I. Dragojevic, J. Dvorak, P. A. Ellison, P. Fallon, M. A. Garcia, J. M. Gates, S. Gros, I. Y. Lee, A. O. Macchiavelli, S. L. Nelson, H. Nitsche, L. Stavsetra, F. S. Stephens, and M. Wiedeking, Phys. Rev. C **80**, 034324 (2009).
[76] C. D. O'Leary, C. E. Svensson, S. G. Frauendorf, A. V. Afanasjev, D. E. Appelbe, R. A. E. Austin, G. C. Ball, J. A. Cameron, R. M. Clark, M. Cromaz, P. Fallon, D. F. Hodgson, N. S. Kelsall, A. O. Macchiavelli, I. Ragnarsson, D. Sarantites, J. C. Waddington, and R. Wadsworth, Phys. Rev. C **67**, 021301(R) (2003).
[77] R. D. Herzberg and P. T. Greenlees, Prog. Part. Nucl. Phys. **61**, 674 (2008).
[78] B. M. Nyakó, F. Papp, J. Gal, J. Molnár, J. Timár, A. Algora, Z. Dombrádi, G. Kalinka, L. Zolnai, K. Juhász, A. K. Singh, H. Hüebel, A. Al-Khatib, P. Bringel, A. Büerger, A. Neusser, G. Schöenwasser, B. Herskind, G. B. Hagemann, C. R. Hansen, G. Sletten, J. N. Scheurer, F. Hannachi, M. Kmiecik, A. Maj, J. Styczeń, K. Zuber, K. Hauschild, A. Korichi, A. Lopez-Martens, J. Roccaz, S. Siem, P. Bednarczyk, T. Byrski, D. Curien, O. Dorvaux, G. Ducheńe, B. Gall, F. Khalfallah, I. Piqueras, J. Robin, S. B. Patel, A. O. Evans, G. Rainovski, A. Airoldi, G. Benzoni, A. Bracco, F. Camera, B. Million, P. Mason, A. Paleni, R. Sacchi, O. Wieland, G. L. Rana, R. Moro, C. M. Petrache, D. Petrache, G. D. Angelis, P. Fallon, I.-Y. Lee, J. C. Lisle, B. Cederwall, K. Lagergren, R. M. Lieder, E. Podsvirova, W. Gast, H. Jäeger, N. Redon, and A. Göergen, Acta Phys. Pol. **B36**, 1033 (2005).
[79] H. Hübel, Acta Phys. Pol. **B36**, 1015 (2005).
[80] B. Herskind, G. B. Hagemann, G. Sletten, T. Døssing, C. R. Hansen, N. Schunck, S. Ødegård, H. Hübel, P. Bringel, A. Bürger, A. Neusser, A. K. Singh, A. Al-Khatib, S. B. Patel, A. Bracco, S. Leoni, F. Camera, G. Benzoni, P. Mason, A. Paleni, B. Million, O. Wieland, P. Bednarczyk, F. Azaiez, T. Byrski, D. Curien, O. Dakov, G. Duchene, F. Khalfallah, B. Gall, L. Piqeras, J. Robin, J. Dudek, N. Rowley, B. M. Nyakó, A. Algora, Z. Dombradi, J. Gal, G. K. andD. Sohler, J. Molnár, J. Timár, L. Zolnai, K. Juhász, N. Redon, F. Hannachi, J. N. Scheurer, J. N. Wilson, A. Lopez-Martens, A. Korichi, K. Hauschild, J. Roccaz, S. Siem, P. Fallon, I. Y. Lee, A. Görgen, A. Maj, M. Kmiecik, M. Brekiesz, J. Styczen, K. Zuber, J. C. Lisle, B. Cederwall, K. Lagergren, A. O. Evans, G. Rainovski, G. D. Angelis, G. L. Rana, R. Moro, W. Gast, R. M. Lieder, E. Podsvirova, H. Jäger, C. M. Petrache, and D. Petrache, Phys. Scr. **T125**, 108 (2006).
[81] G. Viesti, M. Lunardon, D. Bazzacco, R. Burch, D. Fabris, S. Lunardi, N. H. Medina, G. Nebbia, C. Rossi-Alvarez, G. de Angelis, M. De Poli, E. Fioretto, G. Prete, J. Rico, P. Spolaore, G. Vedovato, A. Brondi, G. La Rana, R. Moro, and E. Vardaci, Phys. Rev. C **51**, 2385 (1995).
[82] A. V. Afanasjev and H. Abusara, Phys. Rev. C **78**, 014315 (2008).
[83] Y. R. Shimizu, J. D. Garrett, R. A. Broglia, M. Gallardo, and E. Vigezzi, Rev. Mod. Phys. **61**, 131 (1989).
[84] T. Bengtsson, I. Ragnarsson, and S. Åberg, Phys. Lett. B **208**, 39 (1988).
[85] A. V. Afanasjev, I. Ragnarsson, and P. Ring, Phys. Rev. C **59**, 3166 (1999).
[86] A. V. Afanasjev and S. Frauendorf, Phys. Rev. C **72**, 031301 (2005).
[87] H. Abusara and A. V. Afanasjev, Phys. Rev. C **79**, 024317 (2009).
[88] J. Dudek, K. Pomorski, N. Schunck, and N. Dubray, Eur. Phys. J **A20**, 15 (2004).
[89] A. V. Afanasjev, Y. Shi, and W. Nazarewicz, Phys. Rev. C **86**, 031304(R) (2012).

[90] N. Schunck, J. Dudek, and B. Herskind, Phys. Rev. C **75**, 054304 (2007).
[91] I. Ragnarsson, Nucl. Phys. A **557**, c167 (1993).
[92] W. Satuła, J. Dobaczewski, J. Dudek, and W. Nazarewicz, Phys. Rev. Lett. **77**, 5182 (1996).
[93] A. V. Afanasjev, chapter 11 in the book "50 Years of Nuclear BCS", (World Scientific Publishing Co, Singapore, 2013), p. 138, see also nuclear theory arkhive arXiv:1205.2134. (2013).
[94] T. Lauritsen, M. P. Carpenter, T. Døssing, P. Fallon, B. Herskind, R. V. F. Janssens, D. G. Jenkins, T. L. Khoo, F. G. Kondev, A. Lopez-Martens, A. O. Macchiavelli, D. Ward, K. S. Abu Saleem, I. Ahmad, R. Clark, M. Cromaz, J. P. Greene, F. Hannachi, A. M. Heinz, A. Korichi, G. Lane, C. J. Lister, P. Reiter, D. Seweryniak, S. Siem, R. C. Vondrasek, and I. Wiedenhöver, Phys. Rev. Lett. **88**, 042501 (2002).
[95] Q. A. Ijaz, W. C. Ma, H. Abusara, A. V. Afanasjev, Y. B. Xu, R. B. Yadav, Y. C. Zhang, M. P. Carpenter, R. V. F. Janssens, T. L. Khoo, T. Lauritsen, and D. T. Nisius, Phys. Rev. C **80**, 034322 (2009).
[96] S. Frauendorf and A. Macchiavelli, Prog. Part. Nucl. Phys. **78**, 24 (2014).
[97] S. G. Frauendorf and J. A. Sheikh, Nucl. Phys. A **645**, 509 (1999).
[98] J. J. Valiente-Dobón, T. Steinhardt, C. E. Svensson, A. V. Afanasjev, I. Ragnarsson, C. Andreoiu, R. A. E. Austin, M. P. Carpenter, D. Dashdorj, G. de Angelis, F. Dönau, J. Eberth, E. Farnea, S. J. Freeman, A. Gadea, P. E. Garrett, A. Görgen, G. F. Grinyer, B. Hyland, D. Jenkins, F. Johnston-Theasby, P. Joshi, A. Jungclaus, K. P. Lieb, A. O. Macchiavelli, E. F. Moore, G. Mukherjee, D. R. Napoli, A. A. Phillips, C. Plettner, W. Reviol, D. Sarantites, H. Schnare, M. A. Schumaker, R. Schwengner, D. Seweryniak, M. B. Smith, I. Stefanescu, O. Thelen, and R. Wadsworth, Phys. Rev. Lett. **95**, 232501 (2005).
[99] P. J. Davies, A. V. Afanasjev, R. Wadsworth, C. Andreoiu, R. A. E. Austin, M. P. Carpenter, D. Dashdorj, P. Finlay, S. J. Freeman, P. E. Garrett, A. Görgen, J. Greene, G. F. Grinyer, B. Hyland, D. G. Jenkins, F. L. Johnston-Theasby, P. Joshi, A. O. Macchiavelli, F. Moore, G. Mukherjee, A. A. Phillips, W. Reviol, D. Sarantites, M. A. Schumaker, D. Seweryniak, M. B. Smith, C. E. Svensson, J. J. Valiente-Dobon, and D. Ward, Phys. Rev. C **82**, 061303 (2010).
[100] M. Matev, A. V. Afanasjev, J. Dobaczewski, G. A. Lalazissis, and W. Nazarewicz, Phys. Rev. C **76**, 034304 (2007).
[101] Y. C. Zhang, W. C. Ma, A. V. Afanasjev, G. B. Hagemann, J. Begnaud, M. P. Carpenter, P. Chowdhury, D. M. Cullen, M. K. Djongolov, D. J. Hartley, R. V. F. Janssens, T. L. Khoo, F. G. Kondev, T. Lauritsen, E. F. Moore, E. Ngijoi-Yogo, S. Ødegård, L. L. Riedinger, S. V. Rigby, D. G. Roux, D. T. Scholes, R. B. Yadav, J.-Y. Zhang, and S. Zhu, Phys. Rev. C **76**, 064321 (2007).
[102] A. V. Afanasjev, J. Phys. G **42**, 034002 (2014).